The Astrophysical Journal, 976:167 (22pp), 2024 December 1 https://doi.org/10.3847/1538-4357/ad74f4

A JWST MIRI MRS View of the η Tel Debris Disk and Its Brown Dwarf Companion

Yiwei Chai[1], Christine H. Chen[1,2], Kadin Worthen[1], Alexis Li[1], Antranik A. Sefilian[3,4], William Balmer[1], Dean C. Hines[2], David R. Law[2], B. A. Sargent[1,2], Mark Wyatt[5], Cicero X. Lu[6], Marshall D. Perrin[2], Isabel Rebollido[7], Emily Rickman[8], and G. C. Sloan[2,9]
[1] William H. Miller III Department of Physics and Astronomy, Johns Hopkins University, 3400 N. Charles Street, Baltimore, MD 21218, USA; mchai3@jhu.edu
[2] Space Telescope Science Institute, 3700 San Martin Drive, Baltimore, MD 21218, USA
[3] Astrophysikalisches Institut und Universitätssternwarte, Friedrich-Schiller-Universität Jena, Schillergäßchen 2–3, D-07745 Jena, Germany
[4] Department of Astronomy and Steward Observatory, University of Arizona, Tucson, AZ 85721, USA
[5] Institute of Astronomy, University of Cambridge, Madingley Road, Cambridge CB3 0HA, UK
[6] Gemini Observatory/NSF's NOIRLab, 670N. A'ohoku Place, Hilo, HI 96720, USA
[7] Centro de Astrobiología (CAB), INTA-CSIC, Camino Bajo del Castillo s/n - Villafranca del Castillo, 28692 Villanueva de la Cañada, Madrid, Spain
[8] European Space Agency (ESA), ESA Office, Space Telescope Science Institute, 3700 San Martin Drive, Baltimore, MD 21218, USA
[9] Department of Physics and Astronomy, University of North Carolina at Chapel Hill, Chapel Hill, NC 27599-3255, USA
Received 2024 June 10; revised 2024 August 20; accepted 2024 August 20; published 2024 November 20

Abstract

We report JWST Mid-Infrared Instrument (MIRI) Medium Resolution Spectrograph (MRS) observations of the β Pic moving-group member, η Tel A, along with its brown dwarf binary companion, η Tel B. Following point-spread-function subtraction, we recover the spatially resolved flux from the debris disk around η Tel A, along with the position of the companion exterior to the disk. We present a new 5–26 μm epoch of spectroscopy for the disk, in which we discover a 20 μm silicate feature, and the first ever 11–21 μm spectrum of η Tel B, which indicates a bare photosphere. We derive a new epoch of relative astrometry for the companion, extending the baseline of measurements to 25 yr, and find that it is currently located near the apocenter of an eccentric long-period orbit. The companion's orbit is close enough to the disk that it should significantly perturb the planetesimals within it, resulting in a detectable mid-IR pericenter glow and near alignment with the companion. Contrary to expectations, however, we find that the disk appears to be axisymmetric and potentially misaligned with the companion in the MIRI MRS data. We posit that this may be due to the presence of an additional, as-yet-undetected ~0.7–30 M_J planet orbiting interior to the disk, with a semimajor axis of ~3–19 au.

Unified Astronomy Thesaurus concepts: Debris disks (363); Brown dwarfs (185); Orbits (1184); Circumstellar disks (235)

Materials only available in the online version of record: data behind figures

1. Introduction

Observations of planetary systems with multiple components offer a valuable opportunity to understand the interplay and mutual influence of objects within the system throughout its evolutionary timeline. Young systems with circumstellar disks (e.g., debris disks) in particular offer an exciting view into the sculpting of disk morphologies due to dynamical interactions in the system. Understanding these dynamically induced disk structures can also aid in inferring the presence of as-yet-undetected planets within systems that have circumstellar disks (M. C. Wyatt et al. 1999; A. M. Hughes et al. 2018; M. Wyatt 2020).

To date, however, there have only been a few observed examples of young debris disk systems with wide-separation binary companions (e.g., HD 106906; V. Bailey et al. 2014; L. Rodet et al. 2017). η Telescopii (henceforth, η Tel), as a relatively young (~23 Myr; E. E. Mamajek & C. P. M. Bell 2014) debris-disk-hosting triple system, therefore offers an interesting target for observational study.

The η Tel system is located 49.5 pc away (Gaia Collaboration et al. 2023), within the β Pictoris moving group, and consists of: (1) η Tel A, an A0V-type primary (N. Houk & A. P. Cowley 1975); (2) η Tel B, an M7/8-type brown dwarf companion at a separation of 4″ (P. J. Lowrance et al. 2000); and (3) HD 181327, an F6-type comoving star at a separation of 7′. The primary is host to an edge-on, north–south-aligned debris disk extending to at least 24 au in the mid-IR (R. Smith et al. 2009). Interestingly, HD 181327 is also host to a well-studied debris disk, albeit one that is face-on (G. Schneider et al. 2006; S. Marino et al. 2016; J. Milli et al. 2023).

The debris disk around η Tel A was first identified based on IRAS measurements, indicating an excess in emission at 12, 25, and 60 μm (D. E. Backman & F. Paresce 1993), for which a dust optical depth was calculated as $\tau = L_{IR}/L_* \approx 3.5 \times 10^{-4}$ (P. J. Lowrance et al. 2000). A 2004 Spitzer Infrared Spectrograph (IRS) observation revealed a largely featureless spectrum from 5 to 35 μm, with the exception of a possible 10 μm silicate feature suggesting the presence of large grains (C. H. Chen et al. 2006). Additionally, the excess emission was found to be best fit by two different temperatures of dust: a "warm" 370 K component and a "cool" 116 K component. However, from the spectrum alone, it was not possible to resolve the degeneracies regarding the spatial structure of the dust (e.g., two dust populations at different locations versus two populations with different grain sizes at the same location). 18.3 μm ground-based imaging with T-ReCs on Gemini South spatially resolved the outer component of the disk (R. Smith et al. 2009). Modeling of the T-ReCs disk images was

consistent with a two-component disk structure comprising an unresolved inner "warm" component inward of ∼4 au (as also inferred by C. H. Chen et al. 2006) and a resolved "cool" component in the shape of a narrow ring centered at 24 au.

High-resolution optical spectroscopy of the η Tel disk using FEROS detected Ca II K absorption lines at ∼-23 km s^{-1} that were attributed to circumstellar gas (I. Rebollido et al. 2018). Far- and near-UV spectroscopy with the Hubble Space Telescope (HST) STIS likewise detected absorption features at -23 km s^{-1} for multiple atomic lines, as well as features at -18 km $^{-1}$ (A. Youngblood et al. 2021). The -23 km s^{-1} and -18 km s^{-1} components were respectively attributed to circumstellar and to interstellar gas. In particular, the blue-shifting of the -23 km s^{-1} absorption features with respect to the star's reference frame was interpreted as indicating gas outflow in a radiatively driven disk wind. However, subsequent work (D. P. Iglesias et al. 2023) tested the posited circumstellar origin of the gas by comparing the η Tel absorption features to those of HD 181327, HD 180575, and ρ Tel—three stars with similar lines of sight. The absorption features at ∼-23 km s^{-1} were found in the Ca II K lines of the three other stars, strongly implying that the η Tel absorption lines attributed to circumstellar gas are instead more likely due to an interstellar cloud traversing η Tel's line of sight.

The brown dwarf companion, η Tel B (aka HR 7329 B), was first discovered with HST NICMOS coronography at a separation of 4″ from the primary (P. J. Lowrance et al. 2000). HST STIS spectroscopy indicated a spectral type of M7-8 (P. J. Lowrence et al. 2000), which was confirmed with *H*-band spectroscopy from the Very Large Telescope (VLT) ISAAC (E. W. Guenther et al. 2001). Although initial attempts to show common proper motion from measurements of the companion's separation and position angle (PA) were inconclusive (E. W. Guenther et al. 2001), additional imaging observations from HST NICMOS and VLT NACO across a baseline of 11 yr between 1998 and 2009 were used to confirm η Tel B's status as a comoving companion (R. Neuhäuser et al. 2011), possibly detecting a small linear change in separation (2.91 ± 2.41 mas yr^{-1}) and finding no change in PA. It was suggested that this indicates the companion is currently located near the apocenter of an inclined and/or eccentric orbit. Magnitude estimates for η Tel B were also used to derive a mass of 20–50 M_J from evolutionary tracks (R. Neuhäuser et al. 2011). No additional companions up to 9″ separation from the primary were detected in the 1998 HST NICMOS and 2004–2008 VLT NACO *H*-band images. Later coronagraphic imaging with SPHERE/IRDIS from 2015 to 2017 likewise did not detect any satellites around the companion itself, placing an upper limit on potential satellites from 3 M_J at 10 au to 1.6 M_J at 33 au (P. H. Nogueira et al. 2024).

Additionally, several attempts have been made to characterize the orbit of η Tel B from its astrometric measurements. An analytical approach assuming a face-on circular orbit gave a companion semimajor axis of $a = 220^{214}_{-84}$ au and a period of ∼2000 yr (R. Neuhäuser et al. 2011); this was refined, given the existence (and thus stability) of the edge-on debris disk around η Tel A, which allows for a potential constraint to be placed on the eccentricity of the companion's orbit. Assuming that η Tel B's apocenter distance is indeed $r_{\rm max} \sim 200$ au, and that it has sculpted the outer edge of the debris disk around η Tel A to be $r_{\rm disk} \sim 24$ au, $e = 0.47$, this gives a semimajor axis $a = 136$ au and an orbital period of $P \sim 1000$ yr (R. Neuhäuser et al. 2011). S. Blunt et al. (2017) used the same 11 yr baseline of astrometric measurements from R. Neuhäuser et al. (2011) to perform an orbital fit using the Orbits for the Impatient algorithm, obtaining median orbital parameters of $a = 192^{+240}_{-67}$ au, $P = 1490^{+3350}_{-710}$ yr, $e = 0.77^{+0.19}_{-0.43}$, and $i = 86^{+10\circ}_{-19}$, with uncertainties at a 68% (1σ) confidence interval. Most recently, the orbit-fitting package `orvara` (T. D. Brandt 2021) was used to derive the companion's orbital parameters from 2015 to 2017 SPHERE/IRDIS observations combined with previous astrometric measurements over a baseline of 19 yr (P. H. Nogueira et al. 2024). This fit reported an inclination of $i = 82^{+3\circ}_{-4}$, a semimajor axis of $a = 218^{+180}_{-41}$ au, and an eccentricity of $e = 0.34 \pm 0.26$. While the orbital inclination has been fairly consistent across the literature, derivations of the companion's semimajor axis and eccentricity remain relatively poorly constrained. To date, the large uncertainties on these two parameters illustrate the challenge of characterizing the orbit of long-period companions, for which astrometric observations may only cover a small fraction of the total orbital period.

In this paper, we present a new observation of the η Tel system with the JWST Mid-Infrared Instrument (MIRI) Medium Resolution Spectrograph (MRS). Section 2 details the observation and processing of the data. Section 3 presents a new epoch of mid-IR spectroscopy for η Tel A and the discovery of a 20 μm silicate feature, dust modeling for the MRS spectrum, and our analysis of the spatially resolved disk. In Section 4, we present the first 11–21 μm spectrum for the brown dwarf companion, η Tel B, finding that the object does not possess a mid-IR excess. In Section 5, we discuss: (1) our new epoch of astrometry for η Tel B from MIRI MRS, which extends the baseline of measurements to 25 yr; and (2) our new orbital derivation for the companion. In Section 6, we consider how dynamical interactions with η Tel B are expected to impact the radial extent and symmetry of η Tel A disk; we suggest that an as-yet-undetected planetary mass may explain the disagreement between our observations and the expected effects from the companion. We summarize our results and state our conclusions in Section 7.

2. Observations and Data Processing

2.1. Data Acquisition

The JWST data presented in this article are obtained from the Mikulski Archive for Space Telescopes (MAST) at the Space Telescope Science Institute. The specific observations analyzed can be accessed via doi:10.17909/0js8-gs60.

As part of GTO Program 1294 (PI: Chen), we used MIRI MRS (M. Wells et al. 2015; I. Argyriou et al. 2023) to observe η Tel A (A0V, $K = 5.01$; N. Houk & A. P. Cowley 1975; R. M. Cutri et al. 2003) on 2023 May 13. MIRI MRS is comprised of four integral field unit (IFU) channels, with a wavelength-dependent field of view (FOV) that increases in size per channel; i.e., the FOV is 3.″2 × 3.″7 for Channel 1, 4.″0 × 4.″8 for Channel 2, 5.″2 × 6.″2 for Channel 3, and 6.″6 × 7.″7 for Channel 4. Each channel is further divided into three gratings, which cover the short (A), medium (B), and long (C) wavelength ranges of the channel. The total wavelength coverage of the instrument is from 4.9 to 28 μm. Since our observation uses all four IFU channels, we also observe η Tel B in Channels 3 and 4, due to their larger FOVs.

To avoid saturation by the primary, we use the FASTR1 readout pattern. For the MRSSHORT detector (comprised of Channels 1 and 2), we use five groups per integration, with 17 total integrations. For the MRSLONG detector (comprised of Channels 3 and 4), we use 17 groups per integration, with six total integrations. From the JWST Exposure Time Calculator (ETC; K. M. Pontoppidan et al. 2016), we expect the signal-to-noise ratio (SNR) for η Tel A using such an observing setup to be $\sim$650 at 5.35 μm (ETC Workbook 171617). As MRS is Nyquist-sampled only at the central wavelengths of the detector, we employ a four-point point-source dither pattern for each exposure, to achieve Nyquist sampling across the detector (D. R. E. Law et al. 2023); this also mitigates effects from bad pixels and cosmic rays. The resulting total exposure time is 1121.116 s for Channels 1 and 2, and 1187.717 s for Channels 3 and 4. At the time of observation, the PA of the aperture used was 283°.

The recommended observing sequence (following K. Worthen et al. 2024) for high-contrast imaging with MIRI MRS is to take a background observation, immediately followed by a science observation, then a calibration star observation. Such an observing sequence enables background and classical reference point-spread function (PSF) subtraction, which are necessary to eliminate background noise and to recover the spatially resolved disk and the brown dwarf companion. It is known that MIRI MRS receives significant background emission across its wavelength range, with contributions from zodiacal light and the Milky Way dominating at $\lambda < 12.5$ μm and contributions from the thermal self-emission of the telescope itself dominating at $\lambda > 12.5$ μm (J. R. Rigby et al. 2023). The behavior of the thermal background shows a time dependency that is currently not well modeled; thus, it is preferable to take background and reference observations close in time to the science observation to perform background subtraction.

Unfortunately, due to the constraints of a GTO program with a fixed amount of telescope time, we took only the science observation for η Tel. Since no dedicated background observation was taken, we searched MAST for a publicly available background observed as close in time as possible to our η Tel observation. We elected to use the SMP-LMC-058 background observation from Program 1532, taken three days before our data, on 2023 May 10. The SMP-LMC-058 background consists of a single exposure with 45 groups per integration for each channel, giving a total exposure time of 124.88 s per channel. This is a much larger number of groups per integration than our η Tel observation, which has five groups for Channels 1 and 2, and 17 groups for Channels 3 and 4.

Likewise, no dedicated PSF reference observation was taken for η Tel. To optimize the PSF subtraction, it is important to use a reference source that is similar in spectral type and brightness to the science target, so that the PSF is measured with a similar SNR. A PSF reference observation of N Car (A0II, $K = 4.218$; N. Houk & A. P. Cowley 1975; R. M. Cutri et al. 2003) had already been taken for this program several months earlier, to enable PSF subtraction for observations of β Pic (K. Worthen et al. 2024). The N Car observation consists of four exposures in a four-point point-source dither pattern, each with five groups per integration for MRSSHORT and 15 groups per integration for MRSLONG. The total exposure time for N Car is 1853.73 s for Channels 1 and 2, and 1764.93 s for Channels 3 and 4. Since N Car is similar in spectral type and magnitude to η Tel A (an A0V star with $K = 5.01$), we elect to use the observation of N Car as a reference for PSF subtraction.

For N Car's background, we use the dedicated β Pic background observation taken as part of the same observing sequence in order to maintain contemporaneity. This background observation consists of two exposures in a two-point dither pattern optimized for extended sources, with the same number of groups per integration as for N Car. This gives a total exposure time of 263.63 s for each of the four channels. Both of these observations were taken on 2023 January 11. A more detailed description of this observing sequence is provided in K. Worthen et al. (2024).

Target acquisition is performed for both η Tel A and N Car using the stars themselves, so that the target is well centered within the FOV. This is done to minimize the difference between the two pointings, since effects like fringing can be corrected with varying degrees of effectiveness, depending on the offset (I. Argyriou et al. 2023).

2.2. Data Reduction

We reduce the raw data using version `1.14.0` of the JWST Spectroscopic Pipeline, with CRDS context `jwst_1223.pmap`. We use the same pipeline setup for the η Tel science, N Car reference, and both background observations. The pipeline comprises three key stages: `Detector1`, `Spec2`, and `Spec3`. The `Detector1` stage applies detector-level corrections to the raw data for each individual exposure by fitting accumulating counts ("ramps") into count rates ("slopes"). Since the background estimates are different, based on the number of groups per integration, with the threshold being at around 20 groups per integration, it is necessary to ensure at this stage that the number of groups per integration being included is the same between our science and science background observations (D. Law, private communication). The SMP-LMC-058 background has 45 groups per integration, which is much higher than both the five groups per integration for Channels 1 and 2 and the 15 groups per integration for Channels 3 and 4 for our η Tel science observation. As such, we customize the `saturation.py` script from the pipeline so that only the first five groups for the MRSSHORT detector (Channels 1 and 2) and the first 15 for MRSLONG (Channels 3 and 4) are used when running `Detector1` on the raw SMP-LMC-058 background data. We also set the jump detection threshold step from 3σ to 100σ to prevent the introduction of artifacts into the calibrated data, which occurs due to an overflagging of jumps in the raw data when using the default pipeline settings.

At the `Spec2` stage, specific instrument calibrations are applied to the individual exposure outputs from `Detector1`, in order to calibrate the data into physical astrometric and brightness units. Additionally, for the background observations, a 1D spectrum is extracted for each exposure. We do not make any changes to the default pipeline settings for this stage.

The `Spec3` stage takes the corrected exposures from `Spec2` and combines the four dither positions per exposure into a single 3D spectral cube, consisting of one wavelength axis and two spatial axes. We build cubes separately for each of the 12 MIRI MRS subbands to avoid averaging different measurements from each of the three wavelength gratings across the four IFU channels. Master background subtraction from the background spectra extracted in `Spec2` is also applied at this stage. In the `cube_build` step, we set the coordinate system

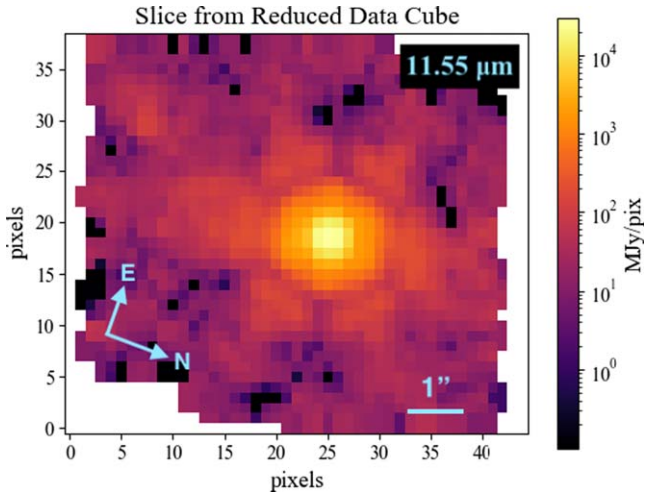

Figure 1. An example slice from the calibrated subband 3A data cube output by Stage 3 of the JWST pipeline, shown with a logarithmic scaling. Note that the six-point PSF dominates most of the FOV. Blacked-out NaN values within the FOV indicate areas of slight oversubtraction due to the pipeline background subtraction.

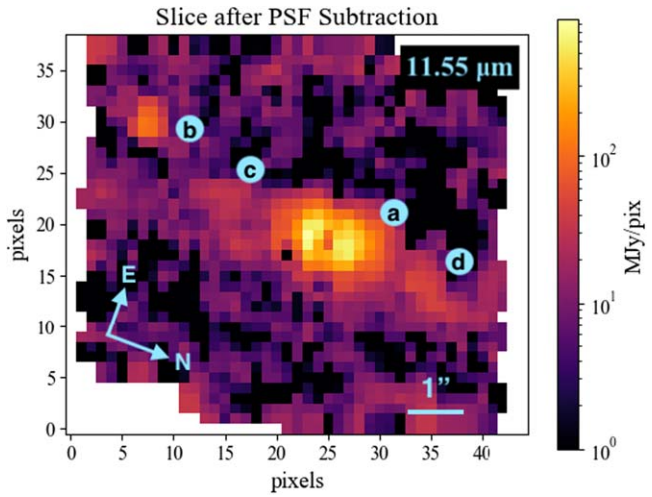

Figure 2. The same wavelength slice shown in Figure 1 after PSF subtraction using N Car, in which the PSF has been scaled to the peak flux of the η Tel slice. The image is log-scaled, so the blacked-out values within the FOV indicate regions of slight oversubtraction. Astronomical objects are labeled: (a) the spatially resolved component of the η Tel A debris disk; (b) η Tel B; (c) background galaxy 2CX0 J192251.5-542530; and (d) an unknown feature (see Section 3.3).

to "`ifualign`" in order to avoid interpolation of the cubes from the instrument to sky frames, as well as to facilitate subsequent PSF subtraction using the science and reference cubes. We build our spectral cubes using the `drizzle` algorithm (D. R. E. Law et al. 2023), retaining the default pipeline pixel sizes for each channel (i.e., 0.″13 for Channel 1, 0.″17 for Channel 2, 0.″20 for Channel 3, and 0.″35 for Channel 4).

2.3. PSF Subtraction

The resolved disk and the companion are both $\sim 10^{-4}$ times fainter in magnitude than the primary star (P. J. Lowrance et al. 2000; R. Smith et al. 2009). Thus, to recover the spatial extent of the debris disk around η Tel A, as well as improve the SNR at which the brown dwarf companion is detected, we perform classical reference PSF subtraction on the calibrated data cubes output by the pipeline. To do this, we calculate the centroids for both η Tel A and N Car by fitting a 2D Gaussian to each wavelength slice in the cubes. Averaging over the centroids for all slices in the cube gives us the final centroid positions for each cube. We then interpolate the N Car cubes to the nearest value, so that the location of the N Car centroid in each slice aligns with that of the η Tel centroid. After scaling the flux of the N Car slices to an η Tel A photosphere model from T. Mittal et al. (2015), we finally perform a slice-by-slice subtraction of the N Car cube from the η Tel cube. We scale the PSF to the η Tel photosphere to obtain the total flux contribution of the disk; however, in using this scaling, we do not see the double-lobed structure reported in R. Smith et al. (2009). We then apply a second PSF scaling, following the method used by R. Smith et al. (2009), in which we scale the flux of the N Car slices to the peak flux of the observed η Tel slices, before subtracting N Car from η Tel. With this scaling, we are able to recover the spatially resolved flux component of the debris disk and identify the two-lobed structure expected from a compact edge-on disk.

Figures 1 and 2 show an example slice of the calibrated MIRI MRS η Tel data before and after the peak-flux-scaled PSF subtraction, with the latter indicating the location of all astronomical objects within the FOV. In both scaling methods, the brown dwarf companion can be seen in the top left corner of the IFU-aligned cubes across subbands 3A–4A ($\sim$11–21 μm). Additionally, using the second scaling method, we detect the presence of background galaxy 2CX0 J192251.5-542530 within the FOV in subbands 1A–3C and a second, previously undetected, extended source, which is likely a background galaxy, in subbands 1A–3A.

The calibrated, PSF-subtracted spectral cubes are the final data products that we use for our following analysis.

3. The η Tel A Debris Disk

3.1. A New Epoch of Mid-infrared Spectroscopy

We extract the η Tel A spectrum over 5–29 μm by performing point-source aperture photometry with the spec3.extract_1d() function of the `jwst` pipeline. We set our aperture radius to be 2.0 × FWHM. As the pipeline-produced spectrum shows slight vertical offsets between the MRS subbands, particularly at longer wavelengths (i.e., Channels 3 and 4), we also perform absolute flux calibration by applying a Relative Spectral Response Function (RSRF), as described by

$$\mathrm{RSRF} = \frac{\text{reference model spectrum}}{\text{reference extracted spectrum}}. \quad (1)$$

For the RSRF, we use N Car to calibrate our observations. We use an N Car photosphere model from K. Worthen et al. (2024) as the model spectrum, and we extract a spectrum from the MRS observations of N Car across Channels 1–4 using the same aperture size as for our η Tel A extraction. We truncate the calibrated spectrum at 25.63 μm, beyond which noise significantly worsens the SNR.

Our calibrated 5–26 μm MIRI MRS spectrum for η Tel A is shown in Figure 3. We find that the MIRI MRS spectrum is consistent with the updated reduction of the 2004 Spitzer IRS spectrum (C. H. Chen et al. 2014), indicating that the disk has not noticeably evolved over time.

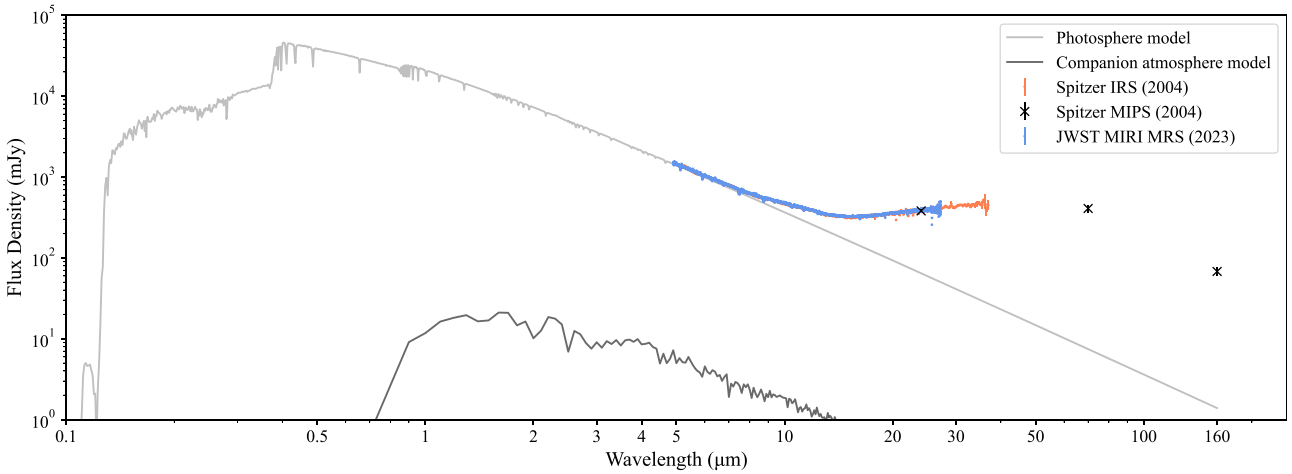

Figure 3. MIRI MRS spectrum of η Tel A, overplotted onto a $T_{\rm eff} = 9700$ K, $\log(g) = 4.0$ photosphere model (T. Mittal et al. 2015). The Spitzer IRS spectrum (C. H. Chen et al. 2014) is shown in orange, along with MIPS photometry (L. M. Rebull et al. 2008). We include our atmosphere model for η Tel B (see Section 5.1) to show that the flux contribution from the companion does not significantly impact the spectrum of the disk, even with the larger Spitzer aperture. The data set used to create this figure is available for download from the online journal.

(The data used to create this figure are available in the online article.)

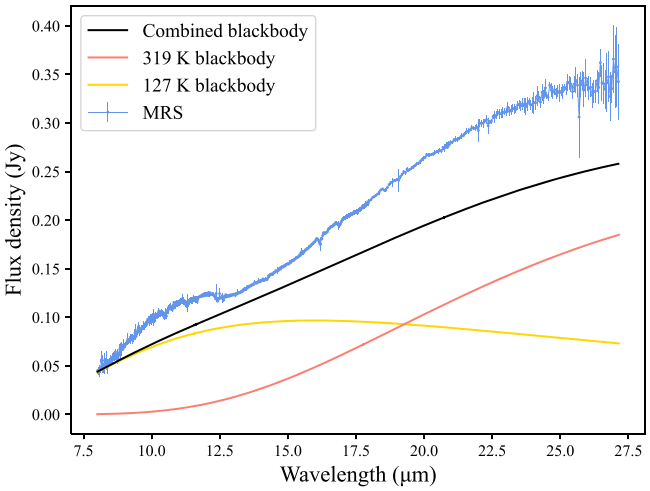

Figure 4. Photosphere-subtracted spectrum of η Tel A, clearly showing the 10 μm feature weakly detected by Spitzer IRS, as well as a broad 20 μm feature detected for the first time in this disk. The best-fit model for the total contribution from the continuum is shown in black; the continuum is best fit by two blackbody components corresponding to a warm dust population with $T_w = 319 \pm 59$ K and a cool population with $T_c = 127 \pm 25$ K. This two-component structure is consistent with previous modeling of the disk (C. H. Chen et al. 2006; R. Smith et al. 2009).

Although the lower angular resolution of the IRS means that the flux of the brown dwarf companion is included in its aperture, we do not consider the IRS spectrum of η Tel A to be significantly impacted by flux from η Tel B, since the primary is at minimum $\sim 10^3$ brighter than the companion over the IRS wavelength range, as indicated by comparison with our atmosphere model for the brown dwarf (see Section 4.1 for modeling details).

Following photosphere subtraction from the MIRI MRS spectrum, we clearly recover the 10 μm silicate feature suggested by C. H. Chen et al. (2006) and identify a broad 20 μm feature for the first time in this disk. Broad spectral features at 10 and 20 μm have been observed in many debris disks and T Tauri stars, with the 20 μm feature being fairly common in cases where a 10 μm feature is present (e.g., C. H. Chen et al. 2006; B. A. Sargent et al. 2009). These two features are indicative of the presence of amorphous silicates, which are known to show broad spectral bands at 10 μm due to Si–O stretching and 20 μm due to O–Si–O vibrations (T. Henning 2010). Indeed, previous modeling of the Spitzer IRS data predicted a 20 μm dust component contribution to the overall spectrum for a composition of large amorphous olivine grains (C. H. Chen et al. 2006), although no such feature was evident in the IRS data, likely due to their lower SNR.

3.2. Dust Modeling

To better understand the disk's spectral features, we perform detailed modeling of the new MIRI MRS spectrum over 7.5–26.9 μm using code originally developed by B. A. Sargent et al. (2009) to model silicate and silica features in the Spitzer IRS spectra of T Tauri stars. We truncate the MRS spectrum shortward of 7.5 μm, as the fitting code attempts to reproduce wiggles in the spectrum at shorter wavelengths created by the incomplete correction of stellar absorption features. We also truncate the spectrum longward of 26.9 μm, as the spectrum becomes substantially noisier at longer wavelengths.

The dusty disk around η Tel is believed to contain dust grains that radiate as a featureless continuum (C. H. Chen et al. 2006). We assume a simplified case of two "bands" of dust populations and set uniform priors on the temperatures of the cold and warm dust populations to $T_c = 80$–200 K and $T_w = 201$–800 K, respectively. These temperature ranges are divided into seven steps (i.e., 17 K and 86 K increments), which are explored over to determine the best fit. We obtain a best-fit warm blackbody dust temperature of $T_w = 319 \pm 59$ K and a cool blackbody dust temperature of $T_c = 127 \pm 25$ K; here, the uncertainties do not represent the 1σ confidence level, but rather the temperature fitting precision, given the prior range on dust grain temperatures and the number of temperature bins used for the fit. Figure 4 shows the warm and cool blackbody components overlaid onto our photosphere-subtracted MRS spectrum to show the contribution of the blackbody continuum to the overall spectrum. We find that the best-fit warm and cool dust temperatures are broadly consistent with those found for the 2004 Spitzer IRS spectrum ($T_w = 370$ K, $T_c = 115$ K; C. H. Chen et al. 2006).

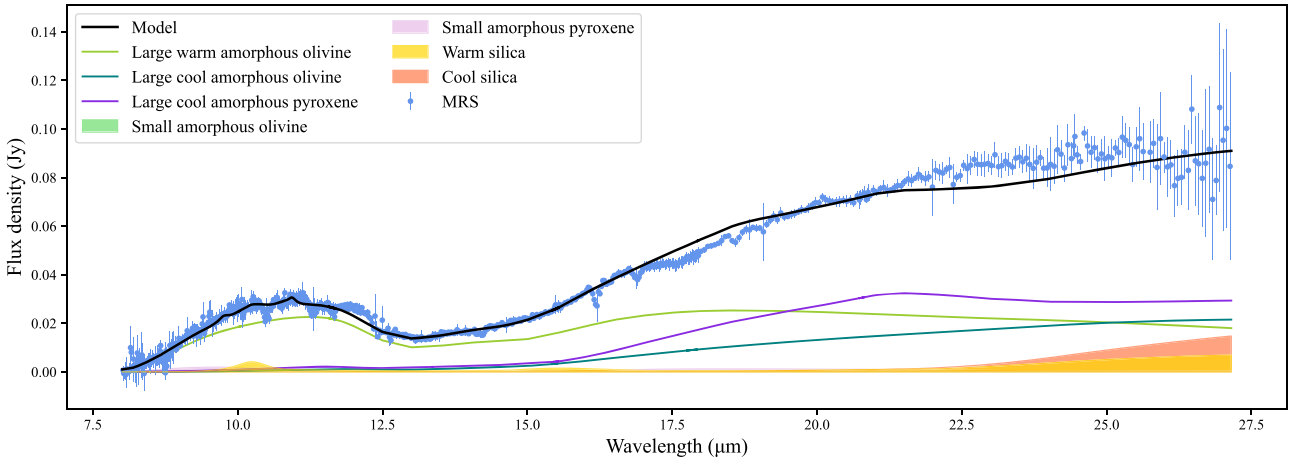

Figure 5. Photosphere + continuum-subtracted spectrum of the η Tel A disk, binned by a factor of 10. There is a firm detection of the 10 and 20 μm dust component features. Modeling indicates the presence of large amorphous olivine and pyroxene grains, as well as some silica, in the disk. The model's difficulty with fitting the tail end of the broad 20 μm feature may be due to the presence of additional components that we do not account for; more detailed modeling outside the scope of this work may help to identify these components.

To more clearly view the spectral features, we then subtract the continuum. Previous modeling of the Spitzer IRS η Tel spectrum suggested that the 10 μm emission was due to the presence of amorphous silicates in the disk's warm dust population (C. H. Chen et al. 2006). Modeling also suggested that the same warm amorphous silicates could give rise to emission at 20 μm, although such a feature was not detected in the Spitzer IRS data.

We model the 10 and 20 μm spectral features and find that large warm amorphous olivine is the primary contributor to the 10 μm feature, consistent with the literature. The broad 20 μm feature, however, appears to be best fit primarily by a combination of large warm and cool amorphous olivine and large cool amorphous pyroxene, with some contribution from warm and cool silica at longer wavelengths. Our best-fit model for the 10 and 20 μm spectral features is shown in Figure 5. The $\chi^2_{\rm red}$ for the entire spectral fit is 3.8. We note that the 20 μm feature appears shifted to a slightly longer wavelength compared to the model. This, along with the presence of some small peaky structures in the 10 μm feature, suggests that there may be additional dust components contributing to the data that we have not presently accounted for in our modeling. More detailed modeling, which is outside the scope of this work, may help to resolve this mismatch between the model and the data.

3.3. The Spatial Distribution of Dust in the Disk

Following PSF subtraction of the science images, we are able to obtain information about the spatial distribution of dust in the disk from 8.67 to 27.89 μm (MRS subbands 2B–4C). By scaling the PSF to the photosphere of the star before subtraction, we can recover the total flux contribution from the dust in the disk. In these images, unresolved excess flux dominates. As a result, we perform a different scaling of the PSF to the peak flux of the science images before subtraction, as in R. Smith et al. (2009), to highlight the spatially extended emission. Figures 6 and 7 show the collapsed-cube images of the disk resulting from these two PSF scalings. We sum up all the wavelength slices in each cube in order to obtain the highest possible SNR.

We assess which features in the cubes are due to real disk morphology and which are due to artifacts. At short wavelengths, we find inconsistent structures close to the location of the star in both scalings; these are likely due to PSF residuals. The ellipsoidal feature in the upper left corner of the Channel 1 and 2 subbands is background galaxy 2CX0 J192251.5-542530. We note the 3σ detection of two small unknown features: one to the immediate right of the primary across across subbands 1A–2A and one in the lower right corner of 1A–1C and 3A. The detection of these features across several subbands makes them unlikely to be due to warm pixels. However, interpreting their spectra has proved challenging, due to their low SNR and the significant discontinuities between subbands; as such, the sources of the two features remain inconclusive.

Emission from the disk itself starts to pick up from $\sim$9 μm (subband 2B) onward. We observe an apparent increase in the radial extent of the disk with wavelength, which has two potential explanations. If real, this could be due to the increased sensitivity at longer wavelengths to cooler dust populations farther out from the star. This may indicate that the η Tel disk possesses a more continuous structure, contrary to the two-component structure suggested by R. Smith et al. (2009), which consists of a narrow ring of material at a fixed distance of $\sim$24 au from the star, along with an unresolved flux component inward of $\sim$4 au. Alternatively, the apparent radial increase could be an artifact introduced by the increase in pixel and PSF size, with wavelength "smearing" the flux from the dust, thus causing it to appear farther out from the star at longer wavelengths.

As resolving this degeneracy will require modeling that is beyond the scope of this work, we focus our considerations on the case for the disk with a two-component structure, as held in the literature (C. H. Chen et al. 2006; R. Smith et al. 2009).

In the second scaling, we also note an apparent increase in the size of an inner cavity between the lobes with wavelength. Since this apparent increase is not observed in both scalings, we conclude it is likely an artifact introduced by the PSF subtraction, due to the increasing pixel and PSF size with wavelength.

4. Does η Tel B have an Infrared Excess?

Since η Tel B is young, and both η Tel A and HD 181327 are known to host debris disks, it is natural to wonder if η Tel B likewise possesses a debris disk. Motivated by this question,

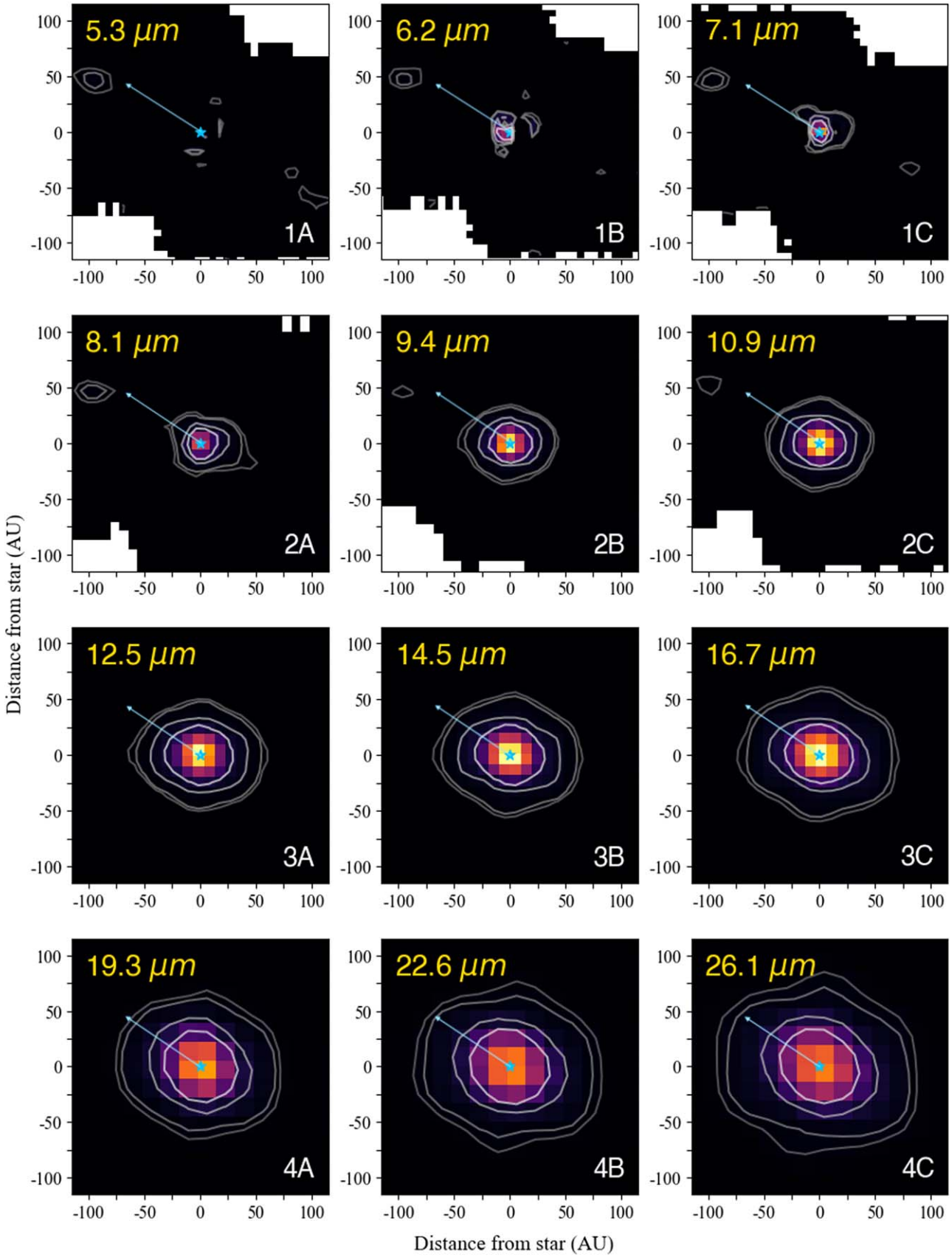

Figure 6. PSF-subtracted, collapsed-cube images of η Tel, in which the PSF was scaled to the photosphere of the star to reveal the total flux contribution from the disk. The images are linearly scaled from 0 to 10^4 MJy sr^{-1} and zoom in on the disk. The contour lines indicate regions at 3σ, 5σ, 20σ, and 50σ detection thresholds for each subband image. The location of the primary is marked with a blue star, and the white arrow indicates the direction of the brown dwarf companion. The wavelength labels give the central wavelengths of each subband to which each image has been collapsed. Note that the radial extent of the disk appears to increase with wavelength.

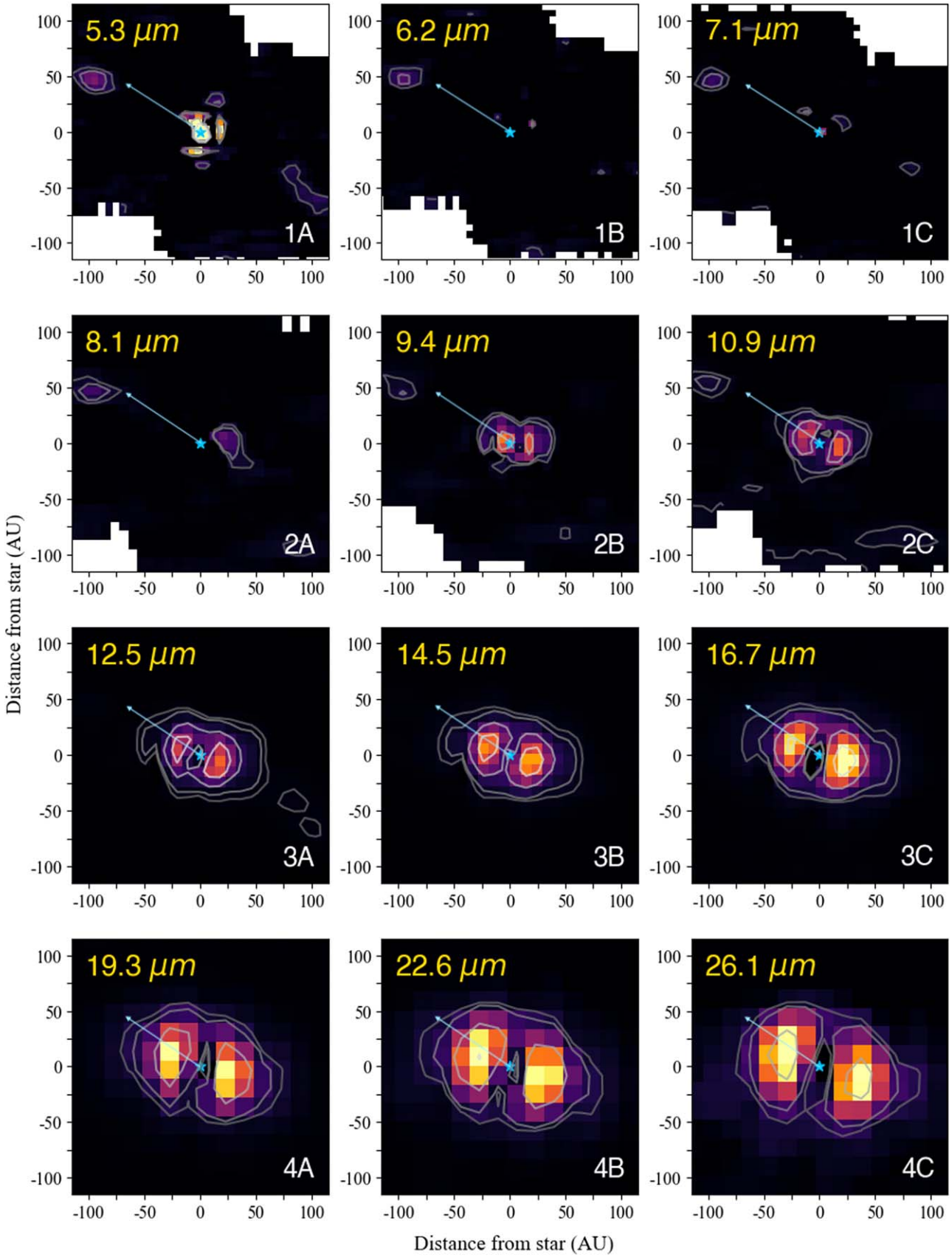

Figure 7. Similar to Figure 6, except the PSF has been scaled to the peak flux of the science image before being subtracted, in order to reveal the spatially resolved dust component. The images are displayed with a linear scaling from 0 to 1.15×10^3 MJy sr^{-1}. We observe that the disk appears largely axisymmetric across all wavelengths and that there appears to be a slight offset in PA between the disk and the position of η Tel B. We also note the apparent increase in the radial extent and inner cavity size of the disk with wavelength. The latter only appears in this scaling and is likely an artifact introduced by PSF subtraction.

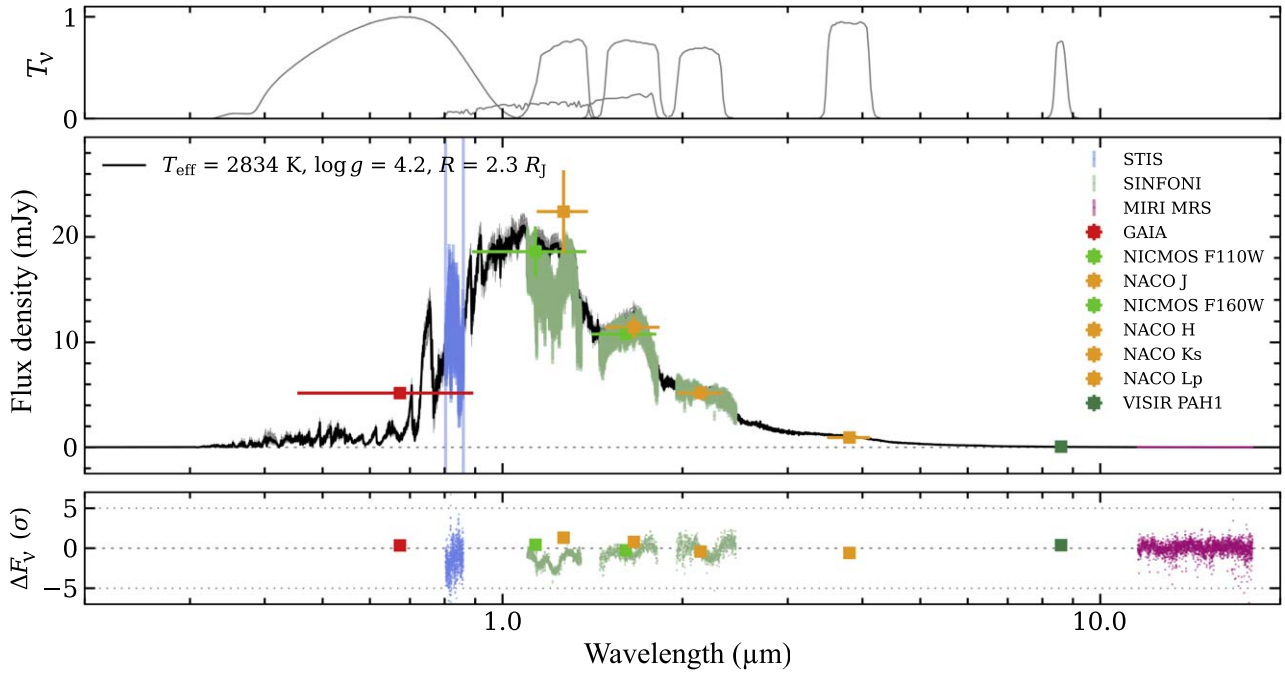

Figure 8. Top: transmission profiles for each photometric filter, indicating flux density throughput versus bandwidth on a normalized scale, where 1 is full flux transmitted and 0 is no flux transmitted. Middle: the full 0.85–21 μm spectral energy distribution of η Tel B, showing existing spectra and photometry along with the new MIRI MRS 11–20 μm spectrum. The black line shows the best-fit atmosphere model for the companion, which was calculated by fitting the spectroscopic and photometric data to a BT-SETTL (CIFIST) model grid using `species` (T. Stolker et al. 2020). The $T_{\rm eff}$, log g, and R values are consistent with expectations for a M7/8-type brown dwarf (see Table 1). Bottom: residual flux density for each data point from the literature compared to the best-fit model in σ. All residuals are within $\pm 5\sigma$, indicating that the model is a good fit to the data.

Table 1
Priors and Best-fit Parameters for η Tel B

Model Parameter	Prior Range	Best Fit
$T_{{\rm eff},B}$ [K]	(2500, 3000)	2830^{+20}_{-30}
log(g)	(3.5, 5.0)	$4.3^{+0.1}_{-0.2}$
R_B [R_J]	(0.5, 5.0)	2.28±0.03
π [mas]	20.6028 ± 0.09	N/A
M_B [M_J]	35 ± 15	29^{+16}_{-13}
log$L_B/L_\odot$	N/A	−2.48±0.01
χ^2_{red}		5.49

Note. Prior ranges in parentheses indicate uniform distributions, and prior ranges for parallax π and companion mass M_B are Gaussian distributions.

we seek to determine if the companion possesses an IR excess at longer wavelengths indicative of the presence of warmed circumstellar dust.

4.1. η Tel B Atmosphere Modeling

To understand the extracted spectrum of η Tel B from the MIRI MRS data, we must first understand the companion's expected atmosphere. We model the atmosphere of η Tel B with the `species` package (T. Stolker et al. 2020), by fitting existing spectra and photometry for the brown dwarf companion to a BT-SETTL (CIFIST) model grid (F. Allard et al. 2011). Our model fit uses spectroscopic measurements from HST/STIS (P. J. Lowrance et al. 2000) and VLT/SINFONI (M. Bonnefoy et al. 2014), as well as photometric measurements from HST/NICMOS H band (P. J. Lowrance et al. 2000) and Gaia G band (Gaia Collaboration et al. 2023). Additionally, we use photometry derived from the observed magnitude difference of η Tel A and B in the following instrument filters: HST/NICMOS F110W (R. Neuhäuser et al. 2011), Paranal/ISAAC K band (E. W. Guenther et al. 2001), Paranal/NACO H, K, and L_p bands (R. Neuhäuser et al. 2011), and VLT/VISIR *PAH* (K. Geißler et al. 2008).

We vary the parameters for $T_{{\rm eff},B}$, log(g), radius, and parallax, setting uniform priors for the first three (Table 1) and Gaussian priors on the parallax and the companion's mass. We assume that the parallax is the same as that for the primary, given as 20.6028 ± 0.09 mas in Gaia EDR3 (Gaia Collaboration et al. 2023). We set a companion mass prior of $M_B = 35 \pm 15\ M_{\rm Jup}$, following R. Neuhäuser et al. (2011).

The data are weighted such that each data set, spectroscopic and photometric, is equal. This prevents each point in the spectroscopic data sets from being weighted equally to each photometric point. We use the nested sampling algorithm `UltraNest` (J. Buchner 2021) to sample 300 live points from the prior. Table 1 summarizes the priors used in our model fitting and the best-fit parameters for η Tel B. The resulting atmospheric model, calculated at the native resolution of MIRI MRS ($R \sim 2700$), is shown in Figure 8 at $R = 1000$.

We note that our derived companion mass of $M_B = 29^{+16}_{-13} M_J$ is lower than the $M_B = 47^{+5}_{-6} M_J$ value obtained by C. Lazzoni et al. (2020) using AMES-COND models (I. Baraffe et al. 2003), although it is consistent when considering both sets of error bars. This discrepancy in mass may be due to the fact that we do not account for the age of the system in our atmospheric modeling.

4.2. η Tel B Spectrum

The detection of warm circumstellar dust around brown dwarfs is dependent on the mass and temperature of the dust,

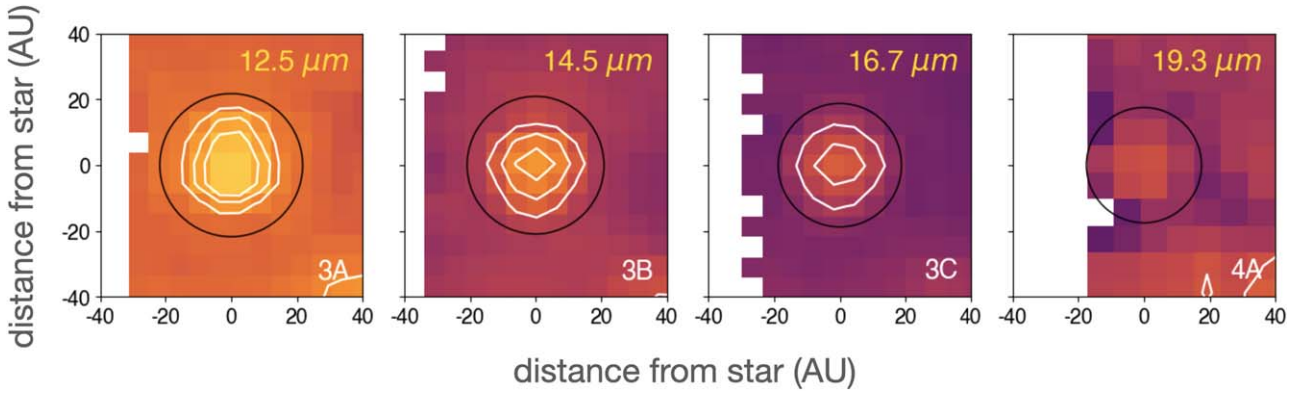

Figure 9. MIRI MRS collapsed subband images of η Tel B from 3A to 4C using a logarithmic scaling. We obtain a 3σ–10σ detection of the brown dwarf across 3A–3C and a 3σ detection in 4A. In subbands 4B and 4C, increased background noise renders the companion irrecoverable; for this reason, we omit these two subbands in our spectral extraction of the brown dwarf. The black circle indicates the size of the extraction aperture.

with submillimeter and millimeter observations being most suited to identifying the presence of traditional 100 au sized debris disks (D. Apai 2013). However, if η Tel B does possess a compact debris disk, we may also be able to detect it via an IR excess across the MRS wavelength range.

To extract an MRS spectrum of η Tel B, we perform aperture photometry at each wavelength slice of the cubes for subbands 3A, 3B, 3C, and 4A. We omit subbands 4B and 4C, as the increase in background noise and lower instrument throughput renders the companion irrecoverable at these longer wavelengths (Figure 9). Since η Tel B is a faint source located at the edge of the MRS FOV, the pipeline does not do a satisfactory job of extracting the spectrum. As such, we manually employ a tapered-column extraction technique for the η Tel B unresolved point source. This involves increasing the aperture size over wavelength to account for the diffraction limit being proportional to wavelength ($\theta = 1.22\frac{\lambda}{d}$). Due to the relative faintness of η Tel B, it is difficult to empirically obtain its FWHM. As such, we use the FWHM calculated for the reference star N Car, since the FWHM of the instrument should behave similarly, irrespective of observing target.

Additionally, if the aperture is too large, it could include additional noise in our extraction. Thus, we restrict the radius of our aperture to be $0.87 \times$ FWHM in Channel 3 and $0.30 \times$ FWHM in Channel 4 (or $\sim 1''$ on-sky for both channels) multiplied by a factor of λ/λ_0, in order to reduce the flux contribution from the background and to improve the SNR of the extraction. We again perform absolute flux calibration and align discontinuities between subbands in the spectra by applying an N Car RSRF; in this case, however, we extract our N Car spectrum across subbands 3A–4A using the same aperture sizes and tapered-column method as for our η Tel B extraction. As the calibrated spectrum remains fairly noisy, particularly for 4A, we bin the spectra for subbands 3A–3C by a factor of 10 and collapse 4A into a single photometric point. We present the final η Tel B spectrum in Figure 10, overplotted onto our atmosphere model (see Section 4.1). To calculate the error bars, we perform an injection recovery test of N Car; this involves scaling N Car to the model flux of η Tel B and injecting it into the η Tel Stage 3 cubes on the opposite side of the primary to η Tel B, before applying PSF subtraction and extracting its spectra using the exact same methods detailed above. Taking the average residuals between the injected and recovered spectrum for each subband gives us the error bars for that subband.

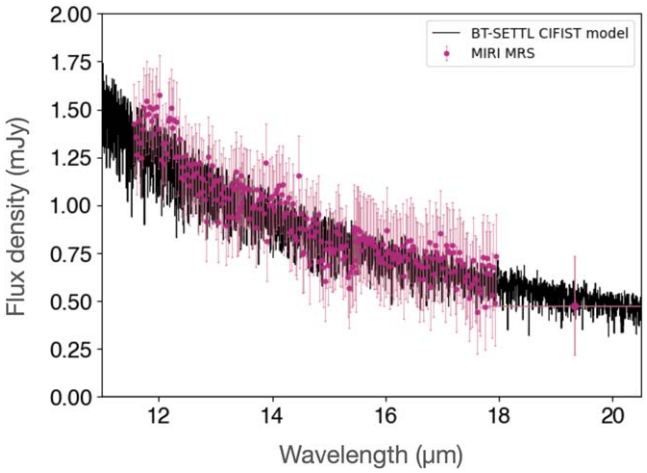

Figure 10. MIRI MRS spectrum of η Tel B, compared to the atmosphere model from Section 4.1. The extracted spectrum is consistent with the model, showing no IR excess. The data set used to create this figure is available for download from the online journal.

(The data used to create this figure are available in the online article.)

Our spectrum shows a good fit to the atmosphere model. This indicates that η Tel B does not possess an IR excess between 11 and 24 μm. We note that this does not necessarily rule out the presence of circumstellar dust around η Tel B; the companion's low luminosity may mean that there is very little dust at 100–260 K temperatures, which would make any excess in the 11–24 μm range simply too faint to be identified by MIRI MRS. However, from our current observations, we conclude that we do not identify the presence of a debris disk around η Tel B.

5. The Orbit of η Tel B

5.1. A New Epoch of Astrometry

The high angular resolution of MIRI MRS allows us to obtain positional accuracy for η Tel A and B to 10 and 23 mas for Channels 3 and 4, respectively (P. Patapis et al. 2024). This enables us to derive a new epoch of relative astrometry, extending the baseline of astrometric measurements by 6 yr since the most recent measurement with VLT SPHERE

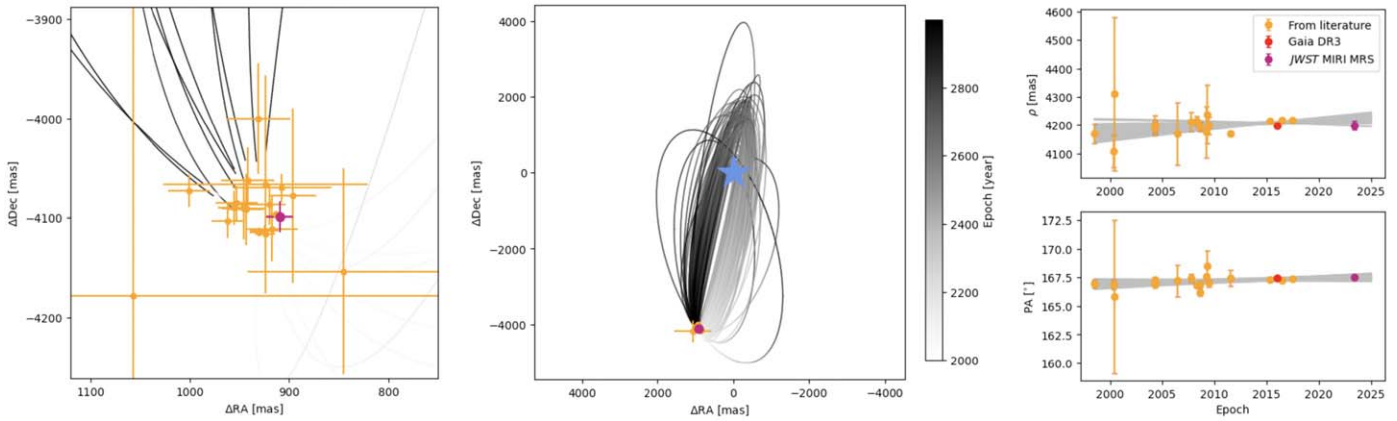

Figure 11. Projected orbits of η Tel B from orbital derivation. Center: on-sky depiction of a sample of 100 potential orbits. The blue star marks the location of the primary and the maroon point marks the current location of the companion from MRS astrometry. Left: close-up of relative astrometry points clustered in the center image. The orange points indicate literature values. Right: separation and PA vs. epoch for the companion with respect to the primary. Due to the long-period nature of the orbit, it is likely that any significant change in separation/PA will not be observable for another few decades.

(P. H. Nogueira et al. 2024) and by 25 yr since the first measurement with HST NICMOS (P. J. Lowrance et al. 2000).

To do this, we fit a 2D Gaussian to the collapsed image of each subband cube from 3A to 4A in order to first identify the pixel coordinates of the η Tel A and B centroids; we exclude the cubes for subbands 4B and 4C, due to higher noise levels increasing the uncertainty in the precise location of the η Tel B centroid. Transforming the pixel coordinates to R.A. and decl. values using the World Coordinate System then allows us to calculate the separation and PA of η Tel B with respect to the primary star. To obtain the final angular separation and PA, we average over the results from subbands 3A–4A, estimating the uncertainties as the standard deviation between the measurements. We calculate a final separation of 4199 ± 15 mas ($\sim$200 au) and a PA of $167.^{\circ}49 \pm 0.^{\circ}18$. As both the primary and companion are observed in Gaia DR3 (Gaia Collaboration et al. 2023), we also use it to calculate the Gaia relative astrometry: $\rho = 4197.3 \pm 3.7$ mas and $\theta = 167.^{\circ}44 \pm 0.^{\circ}09$. Our new astrometric measurements are shown in Figure 11 (right panel), alongside all previous relative astrometry reported in the literature (P. J. Lowrance et al. 2000; E. W. Guenther et al. 2001; K. Geißler et al. 2008; R. Neuhäuser et al. 2011; J. Rameau et al. 2013; P. H. Nogueira et al. 2024) and our calculated relative astrometry from Gaia.

We observe no significant change in separation or proper motion. The new MIRI MRS measurements for both separation and PA are consistent with η Tel B being a common proper-motion companion to η Tel A, located at or near the apocenter of a long-period orbit. This confirms previous analysis (R. Neuhäuser et al. 2011).

5.2. Orbit Fitting

To better characterize the orbital properties of η Tel B, and to understand any potential companion–disk interactions, it is necessary to first understand the orbit of η Tel B. We perform an orbital fit for the brown dwarf companion with the Python package `orbitize!` (S. Blunt et al. 2020), using relative astrometry and stellar absolute astrometry from the DR3 Hipparcos–Gaia Catalog of Accelerations (HGCA; T. D. Brandt 2021). Additionally, although HARPS radial velocity (RV) data exist for η Tel A (T. Trifonov et al. 2020), the primary shows a high-rms RV scatter of 12.805 ± 0.007 km s^{-1}, due to its A0V spectral type, youth, and fast rotation. This makes it difficult to obtain meaningful constraints from the RV data. As such, we omit RV data from our orbital fit for the companion.

Table 2
Median `orbitize!` Posteriors for η Tel B

Parameter	Value	Prior
a_B [au]	142^{+18}_{-11}	Log uniform
e_B	0.5 ± 0.1	Uniform
i_B [°]	79^{+5}_{-6}	Sine
ω_B [°]	169^{+23}_{-21}	Uniform
Ω_B [°]	169^{+3}_{-2}	Uniform
τ_B	0.5 ± 0.1	Uniform
$r_{\mathrm{min},B}$ [au]	71^{+9}_{-6}	…
$r_{\mathrm{max},B}$ [au]	213^{+27}_{-17}	…
t_B [yr]	1100^{+230}_{-132}	…
M_B [M_J]	35^{+7}_{-8}	Uniform
M_A [$M_\odot$]	2.09 ± 0.03	Gaussian
π [mas]	20.61 ± 0.07	Gaussian

We run a parallel-tempered Markov Chain Monte Carlo (MCMC; D. Foreman-Mackey et al. 2013; W. D. Vousden et al. 2016) algorithm with 10 temperatures, 500 walkers, and 10^6 steps, burning the first 100 steps and thinning every 1000 steps; we select these MCMC parameters to maintain consistency with those used by P. H. Nogueira et al. (2024). We set normal priors on the stellar mass ($2.09 \pm 0.03 M_\odot$; S. Desidera et al. 2021) and parallax of the system ($\pi = 20.6028 \pm 0.0988$ mas; Gaia Collaboration et al. 2023), as well as a uniform prior on the companion mass (0.019–0.048 $M_\odot$, i.e., 20–50 M_J; R. Neuhäuser et al. 2011). Uninformative priors are adopted for all other orbital elements; we use the `orbitize!` defaults given in Table 2. We calculate posteriors for nine parameters–six orbital parameters: semimajor axis a_B, eccentricity e_B, inclination i_B, argument of pericenter ω_B, longitude of ascending node Ω_B, and epoch of pericenter τ_B—as well as stellar mass, companion mass, and parallax. Table 2 gives the full list of our derived orbital parameters to 1σ uncertainties. We also do not specify initial positions for the MCMC chains, instead using the `orbitize!` default, which randomly determines the

initial position of the walkers such that they are uniformly distributed across the prior phase space. To test for convergence, we check trace plots and posterior histograms for each parameter.

We obtain best-fit median values of semimajor axis $a_B = 142^{+18}_{-11}$ au, eccentricity $e_B = 0.50^{+0.1}_{-0.1}$, and inclination $i_B = 79^{+5}_{-6}°$. This gives an apocenter distance of $r_{\max,B} = 213$ au, a pericenter distance of $r_{\min,B} = 71$ au, and an orbital period $t_B \sim 1100$ yr. A lack of significant change in orbital motion across 25 yr of observations is therefore reasonable, as we have only observed ∼2% of the companion's total orbit. Figure 11 shows a sample of 100 potential orbits, as well as the corresponding projected change in separation and PA for each of these 100 orbits. Due to the long-period nature of η Tel B's orbit, it will be difficult to observe any significant changes within the next decade; placing more robust constraints on the companion's orbital parameters may not be possible until several decades from now.

We note that while our values for a, e, and i are in agreement with the orbital parameters inferred by R. Neuhäuser et al. (2011), our values for a and e differ considerably from those derived by P. H. Nogueira et al. (2024) using `orvara` (T. D. Brandt 2021). To investigate the potential reasons for this discrepancy, we perform several additional `orbitize!` fits using: (1) their Gaussian prior on the companion mass of $47 \pm 15\ M_J$; (2) only their relative astrometry data; and (3) their initial distribution values. Corner plots for these additional fits are shown in Appendix A. We find that the originally derived parameters for a and e remain robust to the change in companion mass prior and the additional Gaia and MIRI MRS relative astrometry points. The fit using the P. H. Nogueira et al. (2024) initial distribution values returns a bimodal posterior distribution for a and, to a lesser extent, e. The taller peaks ($a \sim 149$ au and $e = 0.5$) are consistent with our posteriors, but the shorter peaks ($a \sim 230$ au and $e \sim 0.3$) are consistent with their results. This suggests that the choice of initial position may have some affect on the posteriors. In particular, instead of using a uniform distribution to set the initial position of the walkers for each parameter, P. H. Nogueira et al. (2024) use a log-normal distribution for the semimajor axis and a normal distribution for all other orbital values. In difficult cases, such as determining a and e for long-period orbits, this may preferentially concentrate exploration of values to those near the chosen initial values. However, we also note that P. H. Nogueira et al. (2024) further constrain the companion's eccentricity to a maximum of e=0.865 to account for the presence of the stable debris disk, which may be an additional explanation for the discrepancy between the two fits.

We additionally acknowledge that the fact that `orbitize!` ! does not exactly reproduce the posteriors from P. H. Nogueira et al. (2024) and consistently has smaller uncertainties than orvara, suggests that some more fundamental difference between the two fitting packages may also be contributing to the different fit outcomes. For example, `orvara` parameterizes e_B as $e_B \sin\Omega_B$ and $e_B \cos\Omega_B$, whereas `orbitize!` does not. Further investigation may provide more illuminating information, but as a deep dive into the workings of both fitting packages is outside the scope of this work, we leave it to future work.

Finally, since observations only cover a small fraction of its total orbital period, its astrometric acceleration between Hipparcos and Gaia in the HGCA has a low significance of 1.96σ for two degrees of freedom (T. D. Brandt 2021). As such, while fitting for stellar absolute astrometry is able to constrain the direction of orbital motion, it is unlikely to provide strong constraints on the dynamical mass of the companion. This is reflected in our median companion mass posterior of $M = 42 \pm 14 M_J$, which appears to be largely prior-driven.

In our following analysis, we assume the best-fit orbital parameters described in Table 2; however, we acknowledge that these parameters may be in part due to the fitting package used and as such also reproduce the analysis using the best-fit parameters from P. H. Nogueira et al. (2024).

6. Discussion

An isolated, nearly edge-on debris disk comprised of planetesimals on circular orbits will feature a symmetric, double-lobed structure. However, dynamical interactions due to the presence of a massive second body in the system can sculpt the structure of the disk, leading to asymmetries (M. C. Wyatt et al. 1999).

In the case of the η Tel AB system, we find that the eccentricity of the companion's orbit ($e_B = 0.50$) corresponds to a pericenter distance of ∼71 au from the primary star (see Table 1). Given the outer disk's radial extent between $r_{\rm in} \sim 22$ and $r_{\rm out} \sim 26$ au (R. Smith et al. 2009), we expect the companion to pass close enough at its pericenter to gravitationally perturb the material within disk over secular timescales.

For low-eccentricity orbits, we can expect secular precession to act on a timescale given by (M. C. Wyatt 2005, see Equations (7) and (8) therein):

$$t_{\rm sec} = \frac{6.15\alpha^{-2.5}\bar{\alpha}^2}{b^{(1)}_{3/2}(\alpha_B)} \frac{0.651 t_B}{\mu}. \quad (2)$$

For higher eccentricities, the above expression should still give a reasonable estimate. In the case of η Tel A and B, the ratio of the perturber to disk semimajor axes is $\alpha = a_d/a_B \approx 24/142 \approx 0.17$, with $\bar{\alpha} = \alpha$, since $a_B > a_d$. The Laplace coefficient is $b^{(1)}_{3/2}(\alpha_B) \approx 3\alpha \approx 0.56$, and the perturber's orbital period in years is $t_B \approx 1100$ yr (see Table 2). We set the ratio of perturber to star masses as $\mu \equiv M_B/M_* = 35 M_J/2.09 M_\odot \approx 0.02$, using the companion mass derived in Section 5.2.

This gives $t_{sec} \approx 1$ Myr. Performing the same calculation using the companion orbital parameters derived by P. H. Nogueira et al. (2024) provides a similar result of $t_{sec} \approx 2$ Myr. Placed into context with the β Pic moving group age of ∼23 Myr, we should expect the observed properties of the η Tel A disk to be consistent with the stable end product of secular interactions with η Tel B, regardless of which fit parameters are used.

We next discuss the predicted disk properties due to dynamical interaction with η Tel B and compare these predictions to the observed MRS data. For our analysis, we consider both our best-fit orbital parameters as well as those derived by P. H. Nogueira et al. (2024).

6.1. Radial Extent of the Disk

In the case of material orbiting a primary star, with a secondary binary companion acting as a perturber on the material, there should be a critical semimajor axis at which the

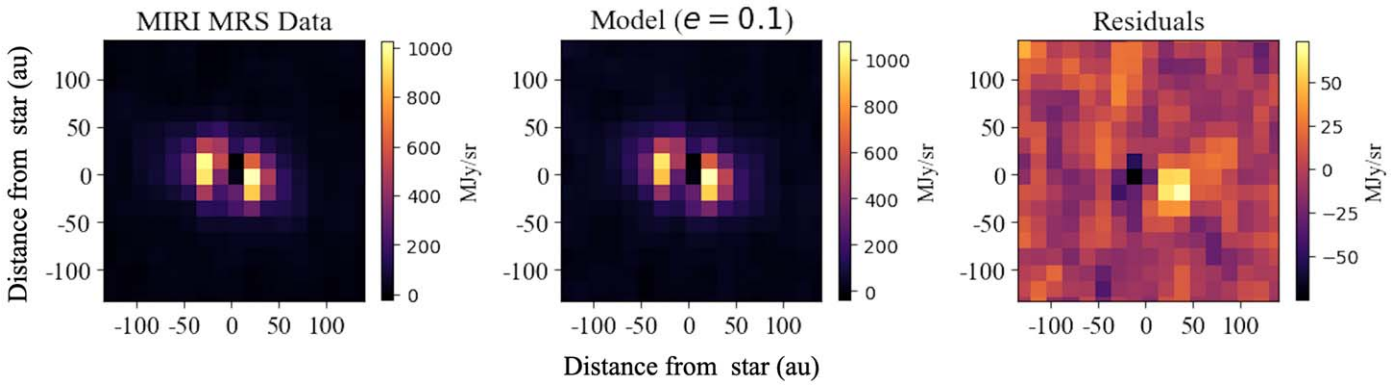

Figure 12. Left: 18 μm slice of MIRI MRS data, following peak-scaled PSF subtraction. Both lobes appear similar in brightness. Center: model of disk with $e_f = 0.1$ that has been convolved with the MIRI MRS PSF at 18 μm, then PSF-subtracted. The pericenter lobe appears slightly brighter. Right: residuals after subtracting the MIRI MRS data slice from the model image, showing remnant structure in the pericenter lobe.

orbit of the material is stable against gravitational perturbations from the companion. M. J. Holman & P. A. Wiegert (1999) empirically derive an expression for this critical semimajor axis, a_c, as a function of the primary–secondary mass ratio, μ, and the semimajor axis, a_B, and eccentricity, e_B, of the secondary perturber's orbit:

$$\begin{aligned} a_c = [&(0.464 \pm 0.006) \\ &+ (-0.38 \pm 0.01)\mu + (-0.631 \pm 0.034)e_B \\ &+ (0.586 \pm 0.061)\mu e_B + (0.15 \pm 0.041)e_B^2 \\ &+ (-0.198 \pm 0.074)\mu e_B^2]a_B. \end{aligned} \quad (3)$$

For η Tel A and B, where $\mu \sim 0.02$, we obtain a critical semimajor axis of $a_c = 26.2$ au. This is comparable to the inferred radial extent of the disk ($r_{\rm out} = 26$ au; R. Smith et al. 2009), suggesting that the observed structure of the disk is consistent with truncation due to the orbit of the brown dwarf companion.

For the P. H. Nogueira et al. (2024) values of $a_B = 218$ au and $e_B = 0.34$, we obtain $a_c = 57$ au. This is greater than the outer radial extent of the disk reported in the literature. However, we note that if the apparent increase in radial extent of the disk seen in the MIRI MRS data is real and not an artifact of PSF subtraction (see Section 3.3, Figures 6 and 7), then at its greatest extent the disk does not seem to exceed ~60 au. This could be consistent with truncation by η Tel B with a larger semimajor axis of ~220 au.

6.2. Symmetry of the Disk

Although an axisymmetric, double-lobed structure is expected for an isolated debris disk, secular perturbations due to the gravitational influence of a second, eccentric body in the system can force the orbit of dust within the disk to become likewise eccentric. This shifts the symmetry of the disk away from the star, resulting in an observable "pericenter glow," as the dust at the forced pericenter of the disk is heated by increased proximity to the stellar host (M. C. Wyatt et al. 1999).

Since a particle's forced eccentricity e_f depends on the eccentricity of the perturber's orbit along with the ratio of its semimajor axis to that of the perturber (M. C. Wyatt et al. 1999, Equation (39)), we estimate the forced eccentricity due to η Tel B as follows:

$$e_f \simeq \frac{5}{4}\frac{a_d}{a_B} \times e_B = \frac{5}{4}\frac{24\ \text{au}}{143\ \text{au}} \times 0.50 \approx 0.1. \quad (4)$$

Here, the perturber semimajor axis, a_B, and orbital eccentricity, e_B, come from our derived orbital parameters for η Tel B. We again take the mean planetesimal belt distance from the star, a_d, to be 24 au (R. Smith et al. 2009). This gives us planetesimal belt apocenter and pericenter distances of 26.5 au and 21.5 au, respectively. We then calculate the grain temperature of the dust at both these distances using the following (C. H. Chen & M. Jura 2001):

$$T_{gr} = 0.707 T_* \sqrt{\frac{R_*}{D_{gr}}}, \quad (5)$$

where D_{gr} is the distance of the grains from the star, $T_* = 9700$ K, and $R_* = 1.7 R_\odot$ (C. H. Chen et al. 2014). This gives a grain temperature of 118 K at the disk's apocenter and 132 K at the disk's pericenter. Taking the ratio of blackbody flux densities across λ_c for each MRS subband, we estimate an expected brightness asymmetry of 96% at 18 μm, which we then divide by a factor of $1 + e_f$ to account for particle bunching at the apocenter (M. Pan et al. 2016). This gives us a final expected brightness asymmetry of 77% at 18 μm, with the pericenter lobe being brighter. It is worth noting that this may be an overestimation of the brightness asymmetry, due to the assumption that the dust is a blackbody; in reality, the temperature of the dust may be hotter. However, given the cool-dust-component temperature of 127 K from dust modeling (see Section 3.2), this would not be a large correction. Likewise, a higher $T_{\rm eff}$ for the primary would give rise to hotter grain temperatures and a smaller brightness asymmetry.

Repeating the above calculations using the best-fit orbital parameters from P. H. Nogueira et al. (2024) produces a forced eccentricity of $e_f = 0.04$, which should produce an 18 μm pericenter brightness asymmetry of ~30%.

Both scalings of the PSF-subtracted MRS data cubes, however, appear largely axisymmetric (Figures 6 and 7), which is inconsistent with expectations of an observable brightness asymmetry. Figure 12 compares an 18 μm slice of the MIRI MRS data (after peak-scaled PSF subtraction) to a model of the disk with $e_f = 0.1$. Subtracting the MIRI MRS data from the model image reveals residuals that indicate the

model is brighter in the pericenter lobe than the data; i.e., the data are less asymmetric than expected from consideration of the system's dynamics. To perform a more rigorous check for potentially fainter asymmetries, we apply angular differential imaging (ADI) to each collapsed subband image of the disk. This is done by rotating the image by 180° and subtracting it from the unrotated image. We also perform the same ADI on the N Car data in order to check whether any potential structures are due to instrument effects. Although we find some asymmetric structure, it is inconsistent across wavelengths and, more critically, appears in both sets of observations. This indicates that these structures are likely caused by the instrument rather than any real physical asymmetry in the η Tel disk. Thus, we find that the η Tel A disk is essentially axisymmetric, contrary to our expectation of an observable disk asymmetry due to gravitational perturbation by η Tel B.

6.3. Mutual Inclination of the Disk and Companion

Secular precession induced by the orbit of η Tel B should cause the orbital planes of the disk and the companion to become aligned; i.e., for a 23 Myr system, we should expect to observe an aligned mutual inclination between the disk and the companion, even if the two were initially misaligned.

The mutual inclination of the disk and η Tel B can be calculated using

$$\cos i_m = \cos i_d \cos i_B + \sin i_d \sin i_B \cos(\Omega_B - \Omega_d), \quad (6)$$

where the i terms are inclinations relative to the sky plane and the Ω terms are the longitudes of the ascending node. For disk and companion parameters of $i_d = 90 \pm 20°$ and $\Omega_d = 172 \pm 1°$ (R. Smith et al. 2009), and $i_B = 79^{+5}_{-6}°$ and $\Omega_B = 169^{+3}_{-2}°$ (see Table 2, Section 5.2), we obtain a mutual inclination of $i_m \sim 11^{+15}_{-14}°$. Thus, we find that the disk and the companion may potentially be misaligned, contrary to expectation. However, further modeling, particularly of the disk's parameters, is needed to improve the uncertainties before we can determine whether or not the disk is truly misaligned with the companion's orbit.

6.4. An Additional Interior Planet?

The absence of compelling evidence for asymmetry in the debris disk, and its potential misalignment with the companion, presents an intriguing puzzle that deserves explanation. Motivated by the work of M. A. Farhat et al. (2023) concerning the HD 106906 debris disk, which is perturbed by both an exterior companion and an inner stellar binary, we propose that our observations could be explained by the presence of additional perturbing masses in the η Tel system. In principle, these masses may include either single or multiple planets interior to the disk and/or the self-gravitational effects of the disk itself, if massive enough. The reasoning behind this is that the presence of such additional masses could counteract the gravitational effects of η Tel B on the debris disk, explaining the identified discrepancies (Sections 6.2 and 6.3).

We consider what may be the simplest scenario: an additional, single, as-yet-undetected planet on a circular orbit completely interior to, and coplanar with, the debris disk (assumed to be massless). It is then possible to constrain the mass m_{pl} and semimajor axis a_{pl} of such a planet using the so-called "Laplace radius" (S. Tremaine et al. 2009; M. A. Farhat et al. 2023). The Laplace radius, denoted by r_L, describes the location where the gravitational perturbations experienced by a planetesimal due to both the inner and outer companions are equal and cancel out. Thus, for a given system, planetesimal dynamics interior (exterior) to r_L will be dominated by the inner (outer) companion, with planetesimals lying in the dominant companion's orbital plane. The Laplace radius, in the limit of $m_{pl} \ll M_*$, can be written as follows (see Equation (1) in M. A. Farhat et al. 2023):

$$r_L^5 = a_B^3 a_{pl}^2 \frac{m_{pl}}{M_B}(1 - e_B^2)^{\frac{3}{2}}. \quad (7)$$

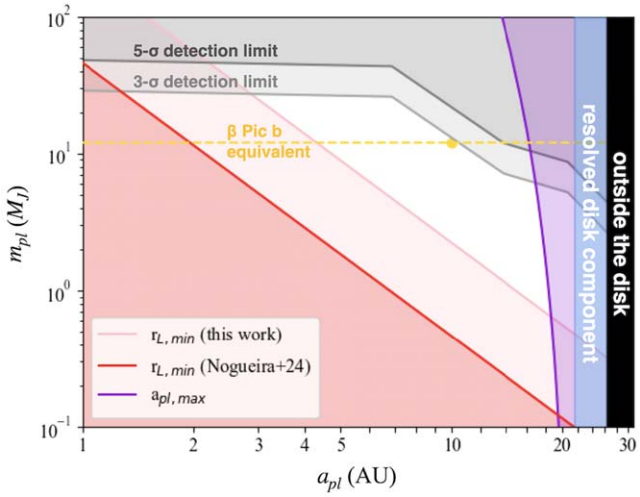

Figure 13. Mass–semimajor axis constraints for a potentially undetected perturbing planet within the disk. The blank white region in the center indicates the possible parameter space for an undetected inner planetary perturber on a circular orbit within the disk plane. The pink lines correspond to the minimum Laplace radius (the r_{out} of the disk; see Equation (7)) and sets the minimum possible mass for the planet at a given semimajor axis a_{pl}. The purple line shows the upper bound on a_p set by the mean motion resonance overlap argument (Equation (9)). The gray lines exclude planets within MIRI MRS 3σ and 5σ detection limits. Note also that the region outside the disk, marked in black, is unstable due to perturbations from η Tel B (Section 6.1).

Since the observed disk structure seems to be inconsistent with that expected based on secular perturbations due to η Tel B alone (Sections 6.2 and 6.3), in Equation (7) we set the minimum Laplace radius to be the disk's outermost radius (i.e., $r_L \geqslant r_{out} \approx 26$ au; R. Smith et al. 2009) and solve for m_{pl} as a function of a_{pl}. The results are shown in Figure 13; a planet whose parameters lie above the light pink line (i.e., values of m_{pl} and a_{pl} for which $r_L \geqslant r_{out}$) could maintain the disk's axisymmetry and its misalignment with the outer companion. We note that using the P. H. Nogueira et al. (2024) orbital parameters to solve for m_{pl} as a function of a_{pl} (shown in dark pink in Figure 13, where again we have set $r_L = r_{out} = 26$ au) results in a larger possible parameter space for an undetected interior planet.

We further constrain the possible parameter space as follows. First, we use MIRI MRS 3σ and 5σ contrast curves to determine the instrument detection limits for potential companions. This allows us to rule out the region of the parameter space as shown using the gray lines in Figure 13. For comparison, we also calculate the expected contrast for a β Pic b–like planet around η Tel using the following equation:

$$f_1 = \left(\frac{d_2}{d_1}\right)^2 \times f_2. \quad (8)$$

We use the β Pic b atmosphere model from K. Worthen et al. (2024) to obtain its flux f_2 at $\lambda_c = 5.3$, 6.2, and 7.1 μm (the central wavelengths of subbands 1A–1C, respectively). The distances of η Tel and β Pic are $d_1 = 47.7$ and $d_2 = 19.44$ pc, respectively. We then divide f_2 by the stellar flux at each wavelength to obtain the final contrasts, finding that MIRI MRS should be able to detect a β Pic b–like planet of $m_{pl} \sim 12 M_J$ at $\geqslant$18 au (within 5σ; and at $\geqslant$12 au within 3σ).

Second, assuming that the inner edge of the disk is carved by the overlap of first-order mean motion resonances due to the planet (e.g., T. D. Pearce et al. 2024 and references therein), the planet's semimajor axis cannot exceed $a_p = a_d - \Delta a_p$. Here, Δa_p is the half-width of the chaotic zone around the planetary orbit given by the following expression (J. Wisdom 1980):

$$\Delta a_p \approx 1.3 \left(\frac{m_p}{M_* + m_p} \right)^{2/7} a_p. \quad (9)$$

This is shown in Figure 13 using a purple curve.

Given these bounds, we are able to rule out certain areas of the planet's possible mass and semimajor axis, as summarized in Figure 13. The central white region therein represents the allowed parameter space for an undetected planet interior to the disk. Looking at Figure 13, it is evident that a planet of mass ~0.7–30 M_J and semimajor axis ~3–19 au may be responsible for the observed disk structure (alternatively, 0.15–40 M_J between 1.5 and 20 au, if using the companion orbital parameters from P. H. Nogueira et al. 2024). That being said, however, we stress that our aim here is not to offer a quantitative prediction but rather to highlight that the observed disk structure is a plausible consequence of the presence of an additional planet.

This is because several additional factors may influence our predictions, which we discuss below. First, the Laplace radius of Equation (7) does not account for potential interactions between the inner and outer perturbers and is instead derived assuming $a_{pl} \ll a_B$. Second, in our calculations, we do not account for nongravitational forces. This is fairly reasonable for millimeter-sized or larger grains; however, the MIRI MRS data trace micrometer-sized grains, which are subject to nongravitational forces, such as radiation pressure and gas drag. Given the system's relatively young age, it is possible for the disk to contain a significant amount of gas (see, however, D. P. Iglesias et al. 2023), which can affect the dust dynamics, such as through migration and the damping of orbital eccentricities/inclinations (T. Takeuchi & P. Artymowicz 2001). If this is the case, then a less massive planet than that identified in Figure 13 would instead be required to produce the same observed structure. Third, we assume that the debris disk is massless, neglecting its (self-) gravitational effects. However, if the disk is massive enough, it may suppress planetesimal eccentricities forced by the eccentric companion (A. A. Sefilian 2024), affecting our inferences. In the extreme case, the disk self-gravity alone, without an additional interior planet, can potentially explain the observed disk structure (K. Batygin et al. 2011; A. A. Sefilian 2024). Regardless, the disk self-gravity, even if not dominant, may well affect our planetary inferences by forcing an inward shift in the Laplace radius (see A. A. Sefilian et al. 2021; M. A. Farhat et al. 2023). Finally, it is important to acknowledge that the inferred parameter space is contingent upon accurate knowledge of the outer companion's orbital parameters. Any updates or improvements to these orbital parameters may necessitate revisions to Figure 13.

7. Conclusions

As part of GTO Program 1294, we present MIRI MRS observations of the η Tel system. Our main findings are:

1. We detect an IR excess in the spectrum of η Tel A, indicating the presence of thermal emission from circumstellar dust. We recover the 10 μm silicate feature and discover a new broad 20 μm silicate feature. Dust modeling suggests the continuum is best fit by two different grain populations at 319 K and 127 K, with the 10 and 20 μm silicate features arising due to the presence of large amorphous grains.
2. We detect the brown dwarf companion η Tel B at a separation of 4″ in MRS subbands 3A to 4A. We calculate a new epoch of astrometry for η Tel B, with $\rho = 4199 \pm 15$ mas and PA $= 167.^\circ36 \pm 0.^\circ19$. Our measurements extend the baseline of astrometric measurements to 25 yr. We detect no significant change in orbital motion.
3. We derive the orbit of η Tel B using relative astrometry and obtain the orbital parameters $a_B = 142^{+18}_{-11}$ au, $e_B = 0.50 \pm 0.1$, and $i_B = 79^{+5\circ}_{-6}$. This gives an orbital period of $t_B \sim 1100$ yr. We find that for our apocenter distance of 214 au, the companion's current location at 209 au validates previous literature suggesting the companion is located at or near the apocenter of a long-period orbit.
4. We present the first 11–21 μm spectrum of η Tel B. We do not detect an IR excess for the object. We perform atmospheric grid model fitting to obtain the following parameters for η Tel B: $T_{\rm eff,B} = 2830^{+20}_{-30}$ K, $log(g) = 4.3^{+0.1}_{-0.2}$, $R = 2.28 \pm 0.03 R_J$, $\log L_B/L_\odot = -2.48 \pm 0.01$, $M_B = 42 \pm 14 M_J$.
5. Using PSF subtraction, we spatially resolve the debris disk around η Tel A from 9.4 to 26.05 μm. We find that the disk has an axisymmetric double-lobed structure across the MRS wavelength range. This is inconsistent with the expected 77% brightness asymmetry at 18 μm due to secular perturbations from η Tel B, assuming our median orbital parameters for the companion.
6. The disk's axisymmetric structure and potential misalignment with the companion may be due to the presence of another mass in the system that is large enough to dominate over secular precessional effects induced by η Tel B. For the case of a single, as-yet-undetected planet, we constrain its mass to be between ~0.7 and 30 M_J, with a semimajor axis within the ~3–19 au range (Figure 13).

Acknowledgments

Y.C. and C.C. acknowledge that this work is based (in part) on observations made with the NASA/ESA/CSA James Webb Space Telescope. The data were obtained from the Mikulski Archive for Space Telescopes at the Space Telescope Science Institute, which is operated by the Association of Universities for Research in Astronomy, Inc., under NASA contract NAS 5-03127 for JWST. These observations are associated with program #1294.

Support for program #1294 was provided by NASA through a grant from the Space Telescope Science Institute, which is operated by the Association of Universities for Research in Astronomy, Inc., under NASA contract NAS 5-03127.

A.A.S. is supported by the Heising-Simons Foundation through a 51 Pegasi b Postdoctoral Fellowship and acknowledges financial support from the Alexander von Humboldt Foundation in the early stages of this work.

Software. This research has made use of the following software projects: Astropy (Astropy Collaboration et al. 2013, 2018, 2022; https://www.astropy.org/), Matplotlib (J. D. Hunter 2007; https://matplotlib.org/), NumPy and SciPy (T. E. Oliphant 2007; https://numpy.org/ & https://scipy.org/), JWST DataPipeline (H. Bushouse et al. 2024; https://jwst-pipeline.readthedocs.io/en/latest/), MultiNest (F. Feroz et al. 2009; https://github.com/farhanferoz/MultiNest), orbitize! (S. Blunt et al. 2020; https://orbitize.readthedocs.io/en/latest/), PyMultiNest (J. Buchner et al. 2014; https://johannesbuchner.github.io/PyMultiNest/pymultinest.html), species (T. Stolker et al. 2020; https://species.readthedocs.io/en/latest/), and the NASA Astrophysics Data System.

Appendix A
Corner Plots

We include corner plots for the spectrum fitting (Figure 14, see Section 4.2) and orbital derivation (Figure 15, see Section 5.2) of η Tel B.

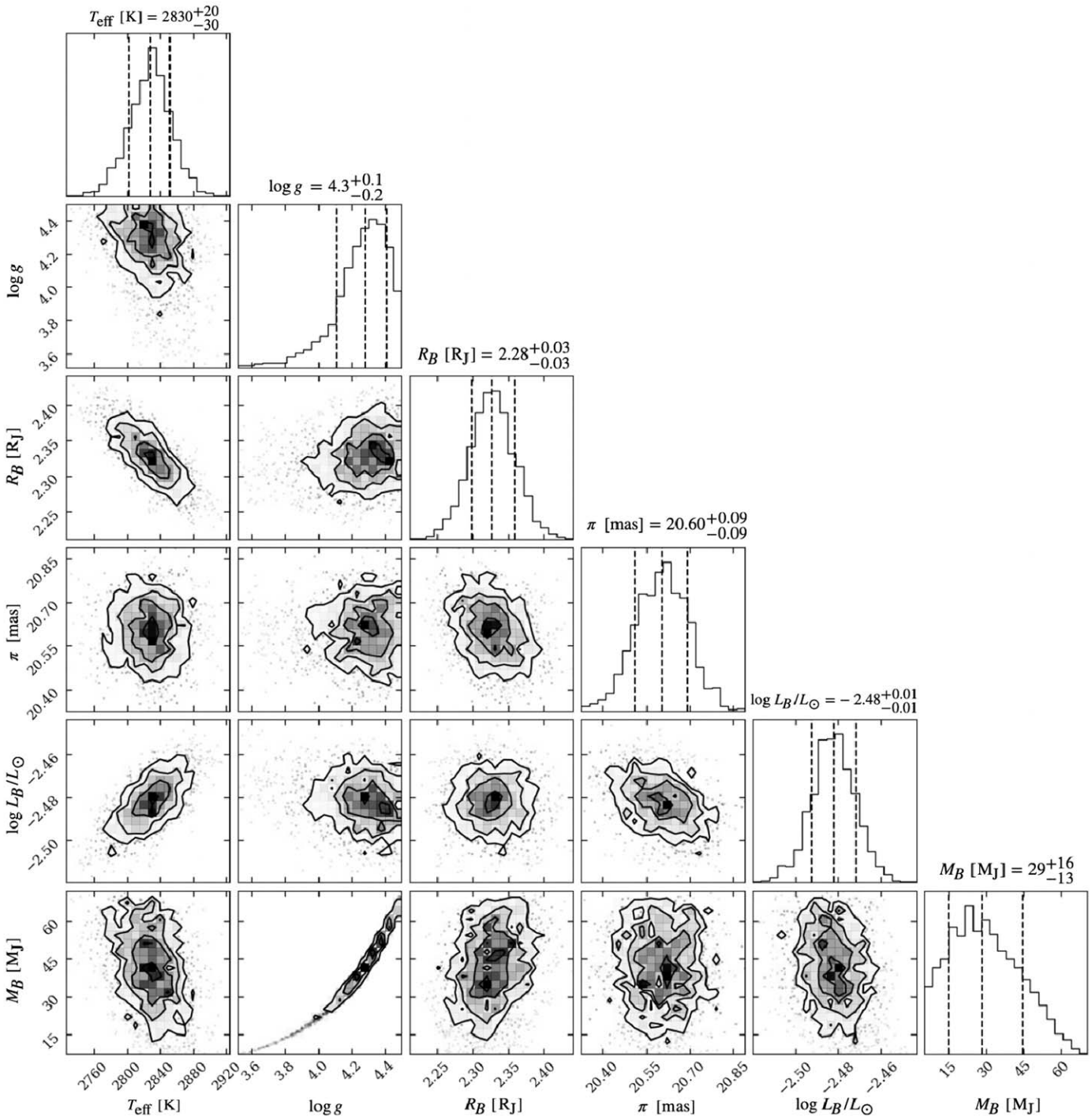

Figure 14. Corner plot for the best-fit properties of η Tel B derived from a BT-SETTL (CIFIST) model grid fit using `species` (T. Stolker et al. 2020).

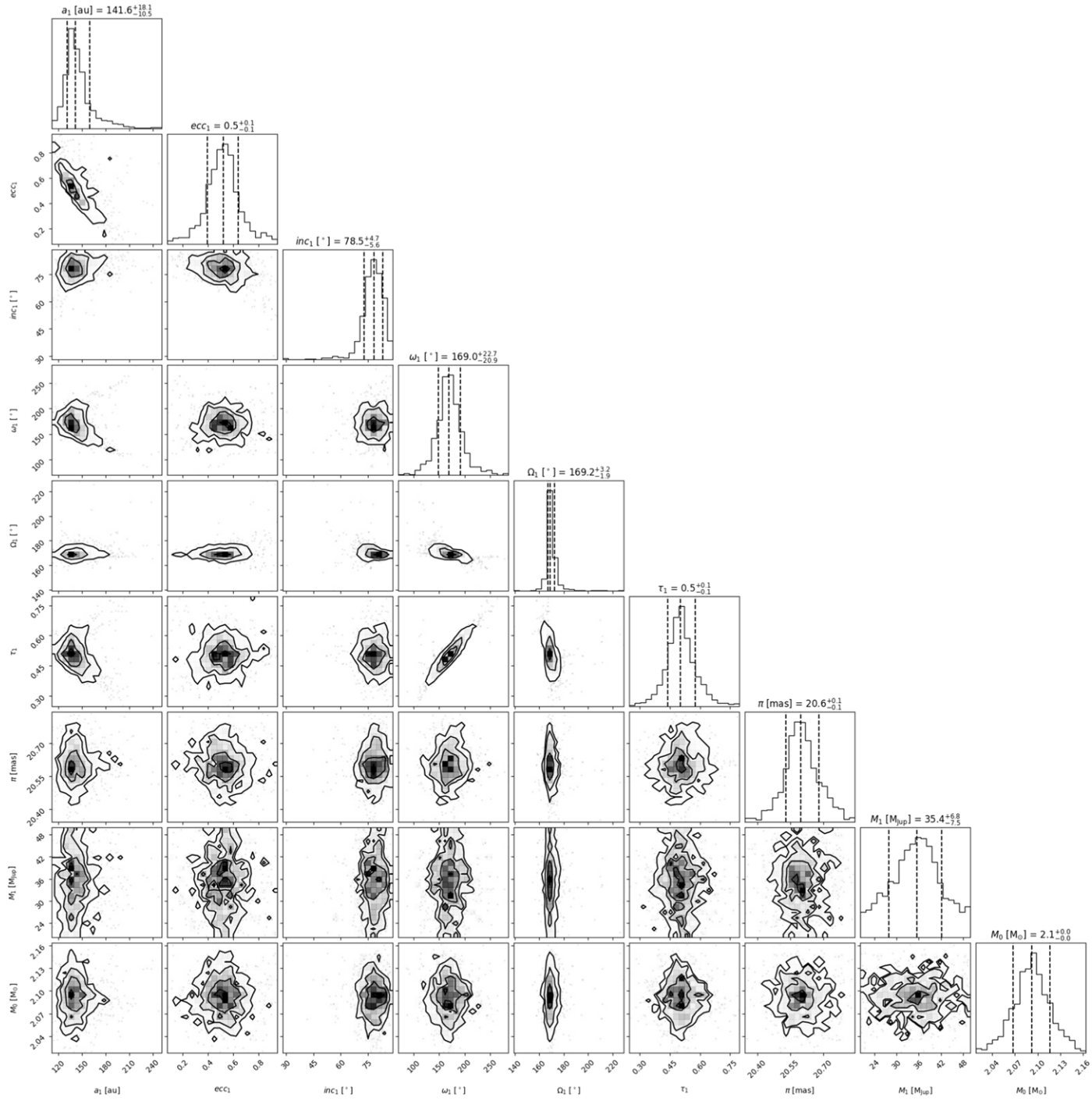

Figure 15. Corner plot for the derivation of the η Tel B orbital parameters using `orbitize!` (S. Blunt et al. 2020), as discussed in Section 5.2.

Appendix B
Additional `orbitize!` Fits for η Tel B

We summarize the variations in orbital results from the different diagnostic fits discussed in Section 5.2 in Table 3 and provide corresponding corner plots (Figures 16–19).

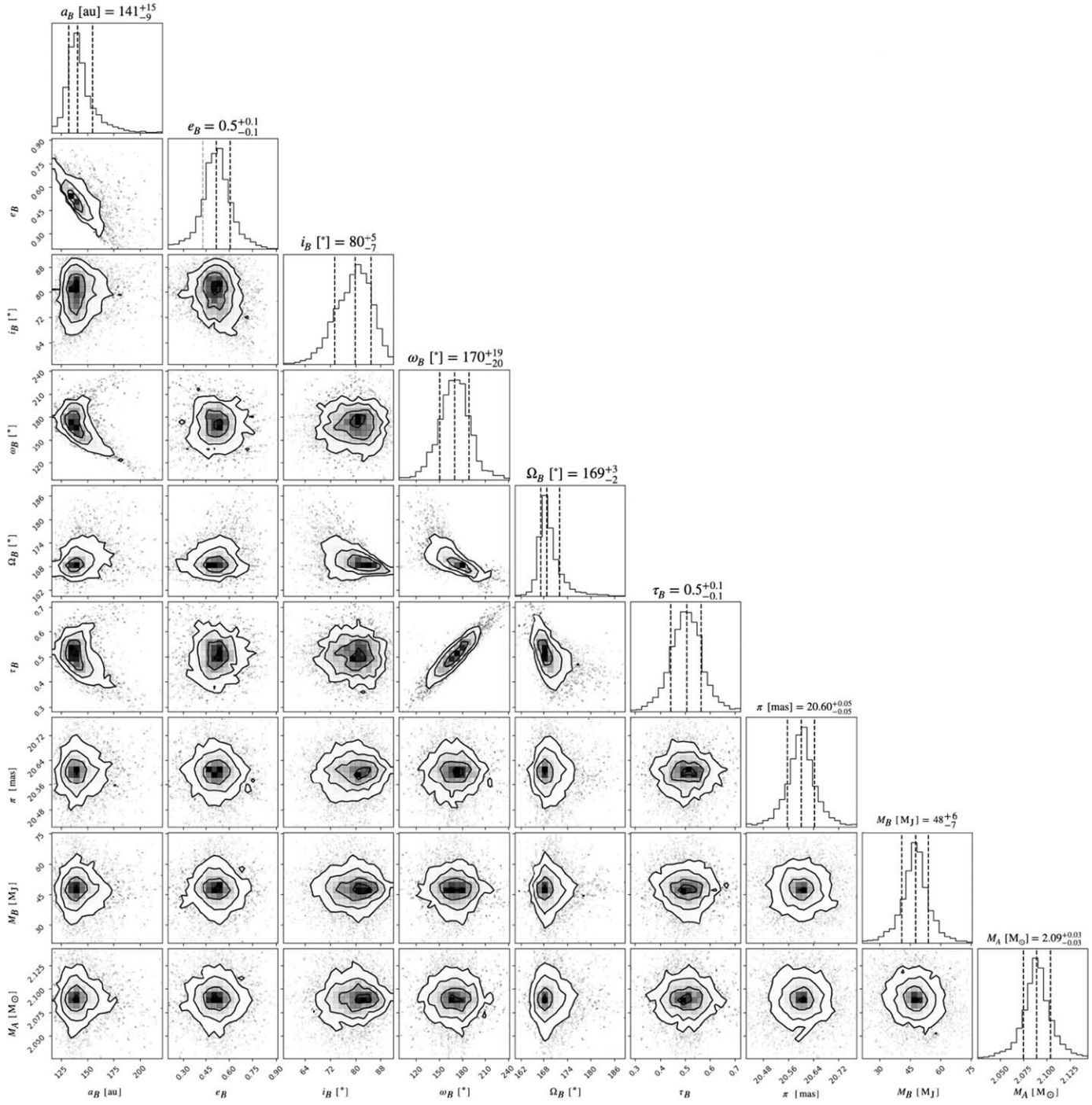

Figure 16. Corner plot for the `orbitize!` (S. Blunt et al. 2020) derivation of the η Tel B orbital parameters using the P. H. Nogueira et al. (2024) companion mass Gaussian prior of $M = 47 \pm 0.15 M_J$.

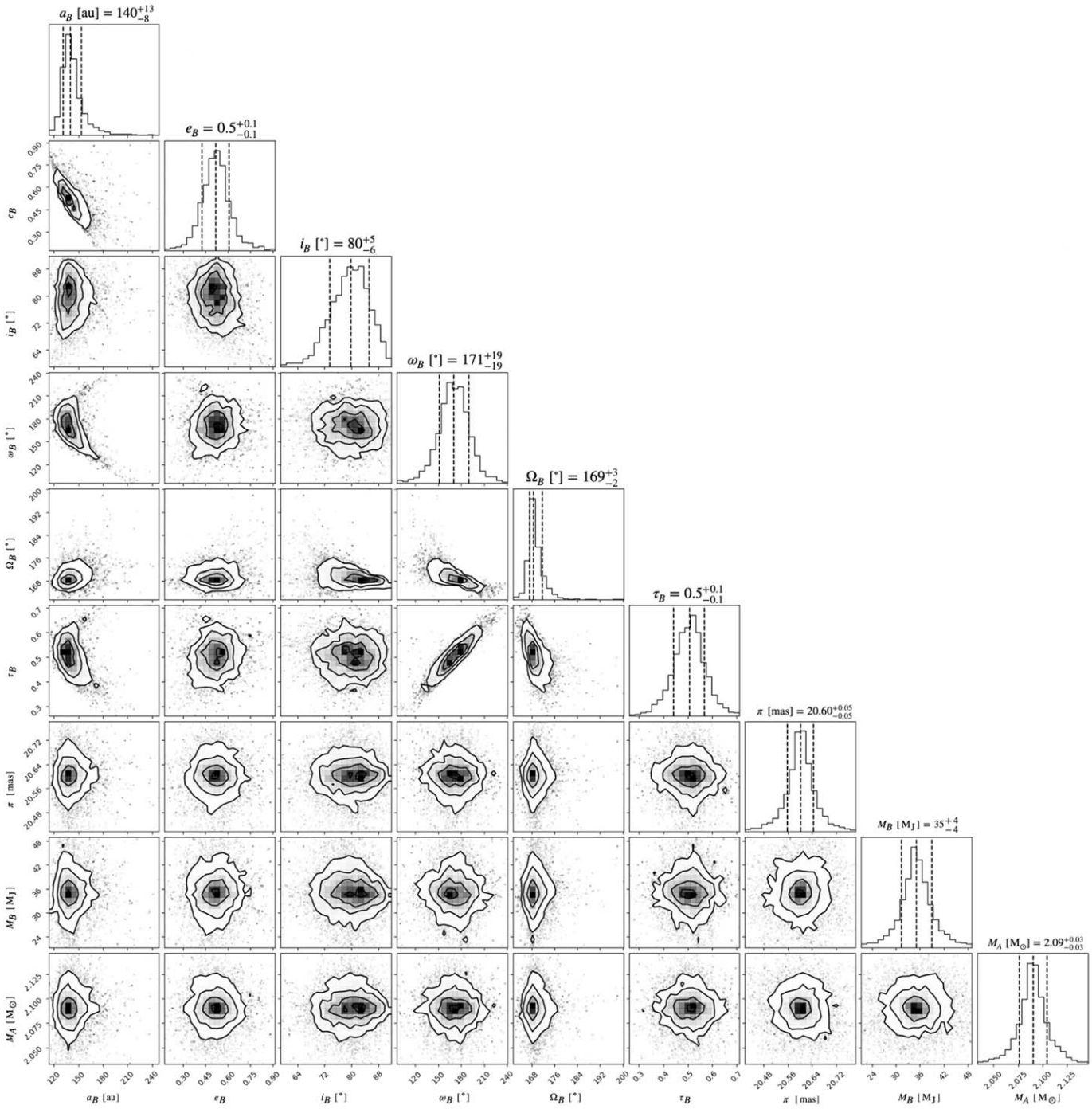

Figure 17. Corner plot for the `orbitize!` (S. Blunt et al. 2020) derivation of the η Tel B orbital parameters using only the relative astrometry included in the P. H. Nogueira et al. (2024) `orvara` fit.

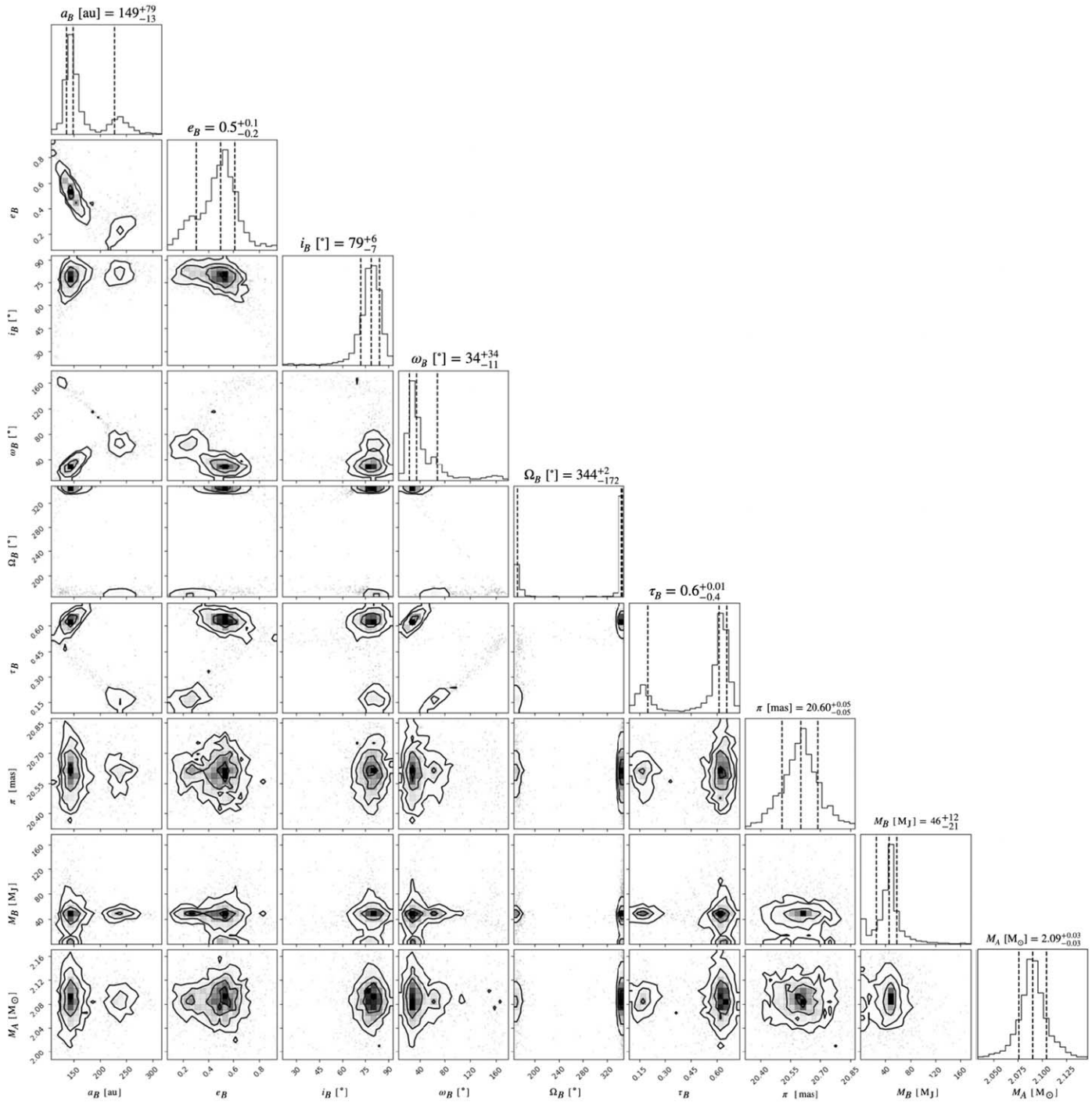

Figure 18. Corner plot for the `orbitize!` (S. Blunt et al. 2020) derivation of the η Tel B orbital parameters using the P. H. Nogueira et al. (2024) initial distribution positions and priors.

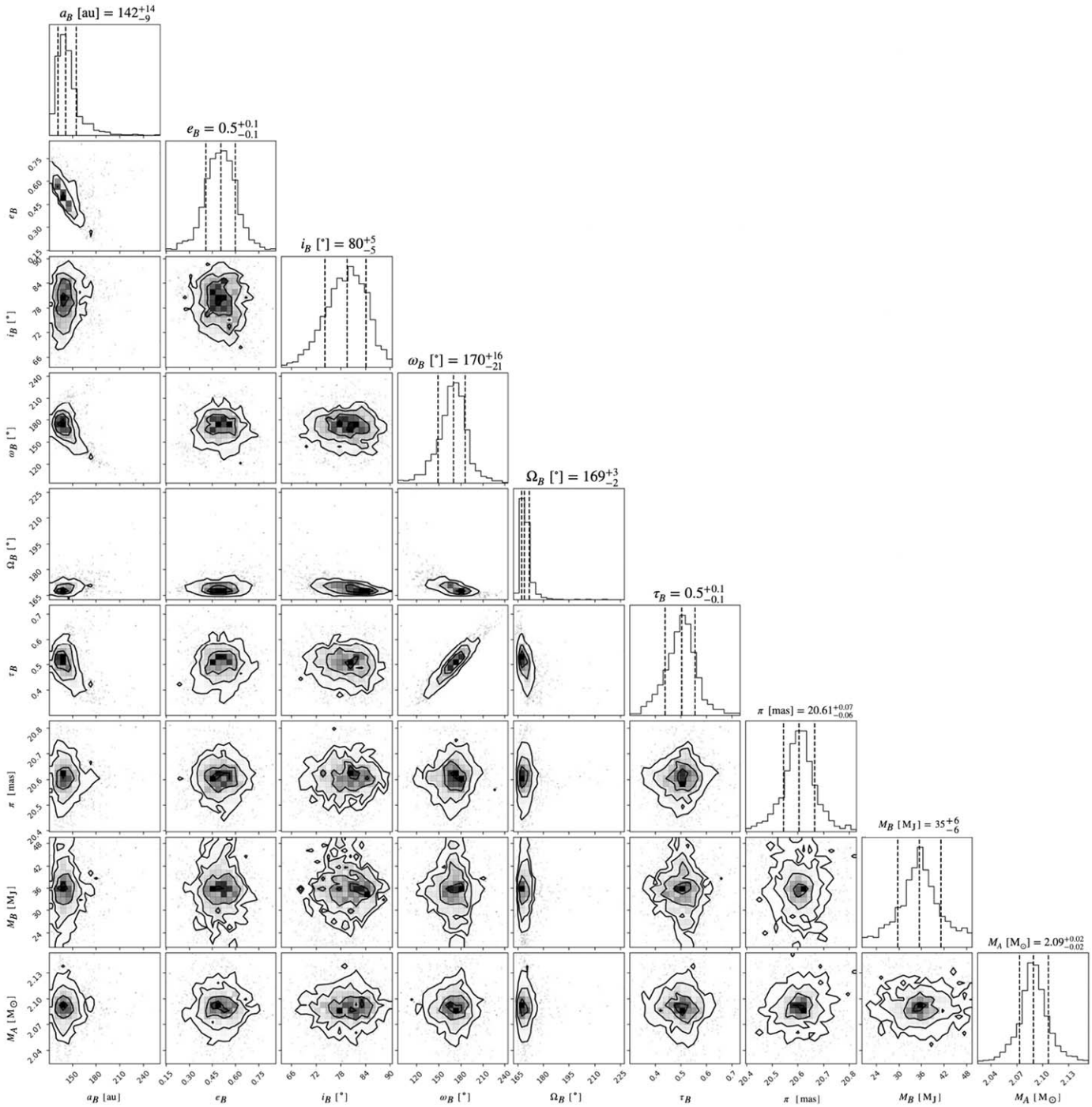

Figure 19. Corner plot for the `orbitize!` (S. Blunt et al. 2020) derivation of the η Tel B orbital parameters using a relaxed primary mass prior of $M = 2.2 \pm 0.1$ (C. H. Chen et al. 2014).

Table 3
Summary of Median `orbitize!` Posteriors for Different Diagnostic Fits

Model Parameter	Section 5.2 Fit	N24 Companion Mass Prior	N24 Relative Astrometry Only	N24 MCMC Initial Positions	Relaxed Primary Mass Prior
a_B [au]	142^{+18}_{-11}	141^{+15}_{-9}	140^{+13}_{-8}	149^{+79}_{-13}	142^{+14}_{-9}
e_B	0.5 ± 0.1	0.5 ± 0.1	0.5 ± 0.1	$0.5^{+0.1}_{-0.2}$	0.5 ± 0.1
i_B [°]	79^{+5}_{-6}	80^{+5}_{-7}	80^{+5}_{-6}	79^{+6}_{-7}	80 ± 5
ω_B [°]	169^{+23}_{-21}	170^{+19}_{-20}	171 ± 19	34^{+34}_{-11}	170^{+16}_{-21}
Ω_B [°]	169^{+3}_{-2}	169^{+3}_{-2}	169^{+3}_{-2}	344^{+2}_{-172}	169^{+3}_{-2}
τ_B	0.5 ± 0.1	0.5 ± 0.1	0.5 ± 0.1	$0.6^{+0.01}_{-0.4}$	0.5 ± 0.1
M_B [M_J]	35^{+7}_{-8}	48^{+6}_{-7}	35 ± 0.4	46^{+12}_{-21}	35 ± 0.6

Note. The uncertainties indicate 68% ranges. The priors for all parameters are the same as described in Table 2, except for the use of a Gaussian companion mass prior in the P. H. Nogueira et al. (2024; N24) Companion Mass Prior and N24 MCMC Initial Positions fits. The initial walker position distributions are all uniform (as described in Section 4.1), except for the N24 MCMC Initial Positions fit, which uses a log-normal distribution for a and a normal distribution for all other parameters.

ORCID iDs

Yiwei Chai https://orcid.org/0009-0008-5865-5831
Christine H. Chen https://orcid.org/0000-0002-8382-0447
Kadin Worthen https://orcid.org/0000-0002-5885-5779
Alexis Li https://orcid.org/0009-0001-7058-8538
Antranik A. Sefilian https://orcid.org/0000-0003-4623-1165
William Balmer https://orcid.org/0000-0001-6396-8439
Dean C. Hines https://orcid.org/0000-0003-4653-6161
David R. Law https://orcid.org/0000-0002-9402-186X
B. A. Sargent https://orcid.org/0000-0001-9855-8261
Mark Wyatt https://orcid.org/0000-0001-9064-5598
Cicero X. Lu https://orcid.org/0000-0001-9352-0248
Marshall D. Perrin https://orcid.org/0000-0002-3191-8151
Isabel Rebollido https://orcid.org/0000-0002-4388-6417
Emily Rickman https://orcid.org/0000-0003-4203-9715
G. C. Sloan https://orcid.org/0000-0003-4520-1044

References

Allard, F., Homeier, D., & Freytag, B. 2011, in ASP Conf. Ser. 448, 16th Cambridge Workshop on Cool Stars, Stellar Systems, and the Sun, ed. C. Johns-Krull, M. K. Browning, & A. A. West (San Francisco, CA: ASP), 91
Apai, D. 2013, AN, 334, 57
Argyriou, I., Glasse, A., Law, D. R., et al. 2023, A&A, 675, A111
Astropy Collaboration, Robitaille, T. P., Tollerud, E. J., et al. 2013, A&A, 558, A33
Astropy Collaboration, Price-Whelan, A. M., Lim, P. L., et al. 2022, ApJ, 935, 167
Astropy Collaboration, Price-Whelan, A. M., & Sipőcz, B. M. 2018, AJ, 156, 123
Backman, D. E., & Paresce, F. 1993, in Protostars and Planets III, ed. E. H. Levy & J. I. Lunine (Tucson, AZ: Univ. Arizona Press), 1253
Bailey, V., Meshkat, T., Reiter, M., et al. 2014, ApJL, 780, L4
Baraffe, I., Chabrier, G., Allard, F., & Hauschildt, P. 2003, A&A, 402, 701
Batygin, K., Morbidelli, A., & Tsiganis, K. 2011, A&A, 533, A7
Blunt, S., Nielsen, E. L., De Rosa, R. J., et al. 2017, AJ, 153, 229
Blunt, S., Wang, J. J., Angelo, I., et al. 2020, AJ, 159, 89
Bonnefoy, M., Chauvin, G., Lagrange, A. M., et al. 2014, A&A, 562, A127
Brandt, T. D. 2021, ApJS, 254, 42
Buchner, J. 2021, JOSS, 6, 3001
Buchner, J., Georgakakis, A., Nandra, K., et al. 2014, A&A, 564, A125
Bushouse, H., Eisenhamer, J., Dencheva, N., et al. 2024, JWST Calibration Pipeline, 1.16.1, Zenodo, doi:10.5281/zenodo.6984365
Chen, C. H., & Jura, M. 2001, ApJL, 560, L171
Chen, C. H., Mittal, T., Kuchner, M., et al. 2014, ApJS, 211, 25
Chen, C. H., Sargent, B. A., Bohac, C., et al. 2006, ApJS, 166, 351
Cutri, R. M., Skrutskie, M. F., van Dyk, S., et al. 2003, yCat, 2246, 0
Desidera, S., Chauvin, G., Bonavita, M., et al. 2021, A&A, 651, A70
Farhat, M. A., Sefilian, A. A., & Touma, J. R. 2023, MNRAS, 521, 2067
Feroz, F., Hobson, M. P., & Bridges, M. 2009, MNRAS, 398, 1601
Foreman-Mackey, D., Hogg, D. W., Lang, D., & Goodman, J. 2013, PASP, 125, 306
Gaia Collaboration, Vallenari, A., Brown, A. G. A., et al. 2023, A&A, 674, A1
Geißler, K., Chauvin, G., & Sterzik, M. F. 2008, A&A, 480, 193
Guenther, E. W., Neuhäuser, R., Huélamo, N., Brandner, W., & Alves, J. 2001, A&A, 365, 514
Henning, T. 2010, ARA&A, 48, 21
Holman, M. J., & Wiegert, P. A. 1999, AJ, 117, 621
Houk, N., & Cowley, A. P. 1975, Catalogue of Two-dimensional Spectral Types for the HD Stars, Vol. 1 (Ann Arbor, MI: Univ. Michigan)
Hughes, A. M., Duchêne, G., & Matthews, B. C. 2018, ARA&A, 56, 541
Hunter, J. D. 2007, CSE, 9, 90
Iglesias, D. P., Panić, O., & Rebollido, I. 2023, MNRAS, 526, 2500
Law, D. R. E., Morrison, J., Argyriou, I., et al. 2023, AJ, 166, 45
Lazzoni, C., Zurlo, A., Desidera, S., et al. 2020, A&A, 641, A131
Lowrance, P. J., Schneider, G., Kirkpatrick, J. D., et al. 2000, ApJ, 541, 390
Mamajek, E. E., & Bell, C. P. M. 2014, MNRAS, 445, 2169
Marino, S., Matrà, L., Stark, C., et al. 2016, MNRAS, 460, 2933
Milli, J., Choquet, E., Tazaki, R., et al. 2023, arXiv:2312.02000
Mittal, T., Chen, C. H., Jang-Condell, H., et al. 2015, ApJ, 798, 87
Neuhäuser, R., Ginski, C., Schmidt, T. O. B., & Mugrauer, M. 2011, MNRAS, 416, 1430
Nogueira, P. H., Lazzoni, C., Zurlo, A., et al. 2024, A&A, 687, A301
Oliphant, T. E. 2007, CSE, 9, 10
Pan, M., Nesvold, E. R., & Kuchner, M. J. 2016, ApJ, 832, 81
Patapis, P., Argyriou, I., Law, D. R., et al. 2024, A&A, 682, A53
Pearce, T. D., Krivov, A. V., Sefilian, A. A., et al. 2024, MNRAS, 527, 3876
Rameau, J., Chauvin, G., Lagrange, A. M., et al. 2013, A&A, 553, A60
Rebollido, I., Eiroa, C., Montesinos, B., et al. 2018, A&A, 614, A3
Rebull, L. M., Stapelfeldt, K. R., Werner, M. W., et al. 2008, ApJ, 681, 1484
Rigby, J. R., Lightsey, P. A., García Marín, M., et al. 2023, PASP, 135, 048002
Rodet, L., Beust, H., Bonnefoy, M., et al. 2017, A&A, 602, A12
Pontoppidan, K. M., Pickering, T. E., Laidler, V. G., et al. 2016, Proc. SPIE, 9910, 991016
Sargent, B. A., Forrest, W. J., Tayrien, C., et al. 2009, ApJ, 690, 1193
Schneider, G., Silverstone, M. D., Hines, D. C., et al. 2006, ApJ, 650, 414
Sefilian, A. A. 2024, ApJ, 966, 140
Sefilian, A. A., Rafikov, R. R., & Wyatt, M. C. 2021, ApJ, 910, 13
Smith, R., Churcher, L. J., Wyatt, M. C., Moerchen, M. M., & Telesco, C. M. 2009, A&A, 493, 299
Stolker, T., Quanz, S. P., Todorov, K. O., et al. 2020, A&A, 635, A182
Takeuchi, T., & Artymowicz, P. 2001, ApJ, 557, 990
Tremaine, S., Touma, J., & Namouni, F. 2009, AJ, 137, 3706
Trifonov, T., Tal-Or, L., Zechmeister, M., et al. 2020, A&A, 636, A74
Vousden, W. D., Farr, W. M., & Mandel, I. 2016, MNRAS, 455, 1919
Wells, M., Pel, J. W., Glasse, A., et al. 2015, PASP, 127, 646
Wisdom, J. 1980, AJ, 85, 1122
Worthen, K., Chen, C. H., Law, D. R., et al. 2024, ApJ, 964, 168
Wyatt, M. 2020, in The Trans-Neptunian Solar System, ed. D. Prialnik, M. A. Barucci, & L. Young (Amsterdam: Elsevier), 351
Wyatt, M. C. 2005, A&A, 440, 937
Wyatt, M. C., Dermott, S. F., Telesco, C. M., et al. 1999, ApJ, 527, 918
Youngblood, A., Roberge, A., MacGregor, M. A., et al. 2021, AJ, 162, 235